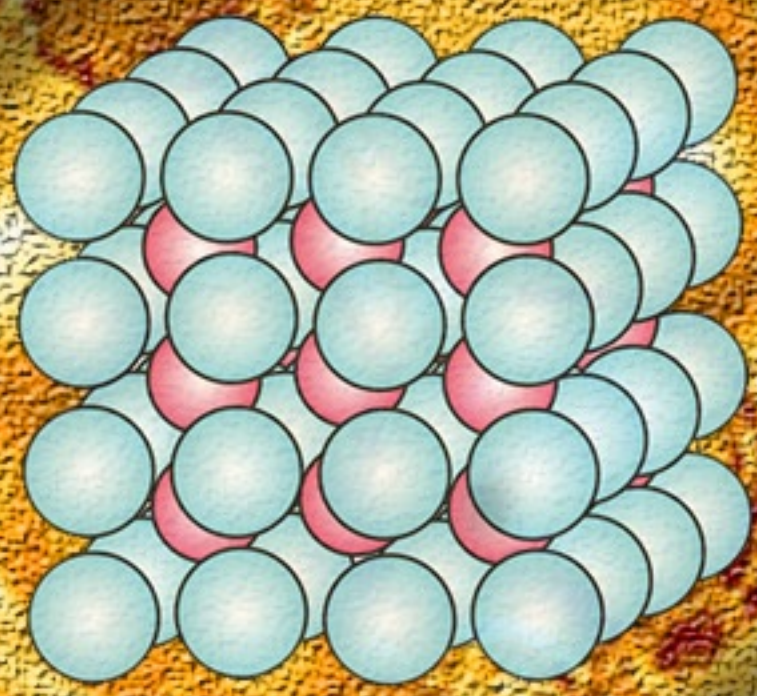
INTERNATIONAL SCIENTIFIC JOURNAL

"MATERIAL SCIENCE"



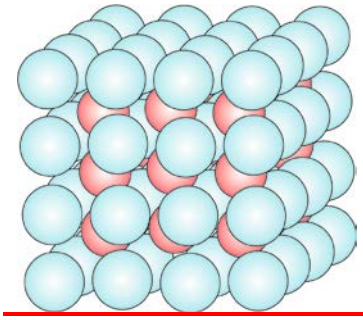
„NONEQUILIBRIUM PHASE TRANSFORMATIONS"

YEAR VII, ISSUE 3/2021

ISSN PRINT 2367-749X
ISSN WEB 2534-8477

PUBLISHER: SCIENTICIC TECHNICAL UNION OF MECHANICAL ENGINEERING INDUSTRY 4.0

108 Rakovski str., 1000 Sofia, Bulgaria
tel./fax (+359 2) 986 22 40, tel. (+359 2) 987 72 90,
office@stumejournals.com, www.stumejournals.com



INTERNATIONAL SCIENTIFIC JOURNAL

MATERIALS SCIENCE. NON-EQUILIBRIUM PHASE TRANSFORMATIONS

PUBLISHER:

SCIENTIFIC TECHNICAL UNION OF MECHANICAL ENGINEERING "INDUSTRY 4.0"

108, Rakovski Str., 1000 Sofia, Bulgaria
tel. (+359 2) 987 72 90,
tel./fax (+359 2) 986 22 40,
office@stumejournals.com

ISSN PRINT 2367-749X, ISSN WEB 2534-8477
YEAR VII, ISSUE 3/2021

EDITORIAL BOARD

CHIEF EDITOR

Prof. Tsanka Dikova, BG

DEPUTY EDITOR:

Dr. Alexander Krugljakow, Germany
Prof. Sergey Dobatkin, Russia
Prof. Sergey Nikulin, Russia
Prof. Victor Anchev, Bulgaria

MEMBERS:

Prof. Adel Mahmud, Iraq
Prof. Anna Proikova, Bulgaria
Prof. Bekir Sami Yilbas, Saudi Arabia
Prof. Dermot Brabazon, Ireland
Prof. Dipten Misra, India
Assoc. Prof.Eugeniy Grigoriev, Russia
Prof. F. W. Travis, United Kingdom
Prof. Gennagiy Bagluk, Ukraine
Assoc. Prof. Ibrahim E.Saklakoglu, Turkey
Prof. Iis Sopyan, Malaysia
Prof. Ivan Parshorov, Bulgaria
Prof. Ivanja Markova, Bulgaria
Prof. Janez Grum, Slovenia
Prof. Jens Bergstrom, Sweden
Prof. Leszek Dobrzanski, Poland
Prof. Ludmila Kaputkina, Russia
Prof. Nikolai Dulgerov, Bulgaria
Prof. Omer Keles, Turkey
Prof. Plamen Danev, Bulgaria
Prof. Rui Vilar, Portugal
Prof. Rusko Shishkov, Bulgaria
Prof. Saleem Hashmi, Ireland
Dr. Sefika Kasman, Turkey
Prof. Seiji Katayama, Japan
Prof. Souren Mitra, India
Dr. Sumsun Naher, United Kingdom
Prof. Svetlana Gubenko, Ukraine
Prof. Sveto Cvetkovski, Macedonia
Prof. Ventsislav Toshkov, Bulgaria
Prof. Yovka Dragieva, Bulgaria

C O N T E N T S

Improving the corrosion resistance of carbon steel cylindrical pipe by nano-materials coating, part -2
1Salloom A. Al-Juboori, Dana Alshamaileh 79

Impostation of an experimental design for studying the optimization of artificial aging process for the aluminium alloys
Irida Markja 85

Nanosized ZnO and ZnO@zeolite composite prepared via sonication method
Gospodinka Gicheva, Neli Mintcheva, Marinela Panayotova 89

Electron Beam Melting and Refining of Copper
Asya Asenova-Robinzonova, Lilyana Koleva, Elena Koleva, Vania Vassileva, Katia Vutova 93

Fabrication of the Porous Structures with Gradient Thickness of the Struts, by using FDM 3D Printing with Dynamically Changed Parameters during the Printing
Nikola Palic, Fatima Zivic, Vukasin Slavkovic, Nenad Grujovic 96

Development and investigation of new special steel
Argirov Christo, Kalchevska Kamelia 100

Technical requirements for the materials from which clothes for firefighters are made. Types of tests
Ivanov Ivan, Nikolova Valentina, Liliq Damyanova 103

Physicochemical and technological researches of marls from the area of the village Lovets related to the production of the new "Yellow paving stones"
Lyuben Lakov, Gergana Mutafchieva, Gabriel Peev, Mihaela Aleksandrova , Bojidar Jivov 107

Set up for real time capturing of welding parameters
Deyan Gradinarov 110

Improving the corrosion resistance of carbon steel cylindrical pipe by nano-materials coating, part -2

[1]Salloom A. Al-Juboori, Dana Alshamaileh
[1]Professor in Mechanical Engineering, B.Sc, M.Sc, PhD, Leeds University, U.K
[1]Engineering Faculty /Mutah University / AlKark/ Jordan, Email: sajibury@mutah.edu.jo

Abstract: *This part is a continuation of Part-1, which was studying the effect of anti-corrosion nano-materials coating using zinc (Zn) and cobalt (Co) on corrosion resistance and its relationship with mechanical properties. While, part 2 was on studying the linear stresses resistance after coating by using the same nanomaterials of paret-1 of carbon steel pipe and their relationship with chemical corrosion resistance using finite element analysis (FEA). The coating was tested with different thicknesses of nano-layers (300 μm, 600 μm, 900 μm, 10 μm) on a thick-walled cylindrical pipe subjected to a uniformly distributed internal pressure of 4 bars. The results showed that the value of linear normal stresses did not change when coating with 300 μm for both nano-coating materials. However, it was started to decrease slightly when covered with 600 μm of cobalt and continues to decrease with increasing the coating thickness. In addition, the results have shown that the overall improvement in linearized normal stresses and corrosion resistance due to cobalt coating can be about (66 %) higher in comparison with Zinc at 10 μm thickness of coating*.

KEYWORDS*: LINEAR STRESSES, NANO-COATING, ZN, CO, AND CARBON STEEL, CORROSION RESISTANCE, ANSYS-19.*

Abbreviations: *ALD: Atomic Laser Deposition, CVD: Chemical Vapor Deposition, ISO: International Organization for Standardization, MWCNT: Multi-Wall Carbon Nanotubes, SEM: Scanning Electron Micrographs, SCC: Stress Corrosion Crack, Co: Cobalt, Ni: Nickel, μm : nanometer, Zn : Zinc, μ: surface Roughness, E: Modulus of elasticity, v: Poisson's ratio, σ: Sigma (tensile stresses),P: Fluid pressure*

Background: The relationship between corrosion and the degradation of metals' mechanical properties is very important factor affecting the metal life. The further corrosion the metal undergoes, and both the tensile strength and fracture strength of the metal are diminished by the corrosion [1,2]. Corrosive wear is also known as chemical wear or oxidation. Which is due to the chemical and electrochemical interaction of the surface and the environment. This form of wear can occur, inn corrosive wear, the fine corrosive products on the surface reflect the wear debris. As the shaped layer is broken or removed by sliding and abrasion because of corrosion, another layer starts to form, and the process of removing a new corrosive layer formation repeated. The most common corrosive media are water, seawater, oxygen, acids, chemicals, atmospheric hydrogen sulfide and sulfur dioxide.

Corrosion can have a variety of negative effects on metal. When metal structures suffer from corrosion, they become unsafe which can lead to accidents, such as collapses. Even minor corrosion requires repairs and maintenance. Corrosive wear can be minimized by selecting the right materials that will resist environmental attack, by applying different coating methods. This can controlling the environment, and reducing operating temperatures in order to lower the rate of chemical reaction [6,7]. Seawater distinguished by being a corrosive complex medium due to the high salt content, dissolved organic substances, such as carbohydrates and amino acids, and dissolved gasses such as (chiefly nitrogen, oxygen, argon, and carbon dioxide). The presence of carbonates, chloride and other component will influence seawater chemistry significantly and lead to the formation of scale at the membranes and in piping structures. This lead to severe corrosion of alloys, especially carbon steel, and with high level of presence of dissolved oxygen, corrosion will accelerate. Figure (1) shows an example of corrosion effect on bolts, valves, flanges, piping, and pipe support [8].

One of the most important problem of damage that contribute to reduce both the static and cyclic strength of a performance of thin-walled structures that immersed in seawater such as pipelines is corrosion problem. It is a process depend on a time, local environment inside or near the pipeline and occur on the internal and external surfaces in the pipe, in the base material and contact welding. As such, protection of metal equipment in a seawater environment will give prime consideration [9].

Predicting the rate of corrosion of a steel structure in seawater is one of the difficult tasks facing design and corrosion engineers. The main parameters that effect on the rate are dissolved oxygen, salinity, temperature, ph and Sulphur [10]. Protective coatings are one of the most important methods used to reduce metal waste caused by surface corrosion, which leads to extend the life of metal equipment. Example of these coatings are Chromized or Aluminized coatings [11]. Chromatid zinc deposits was given a better protection against corrosion compared to unprotected zinc that was corrodes quickly in chloride medium [12]. In present work a more advanced coating will be used which is a Nano-coating.

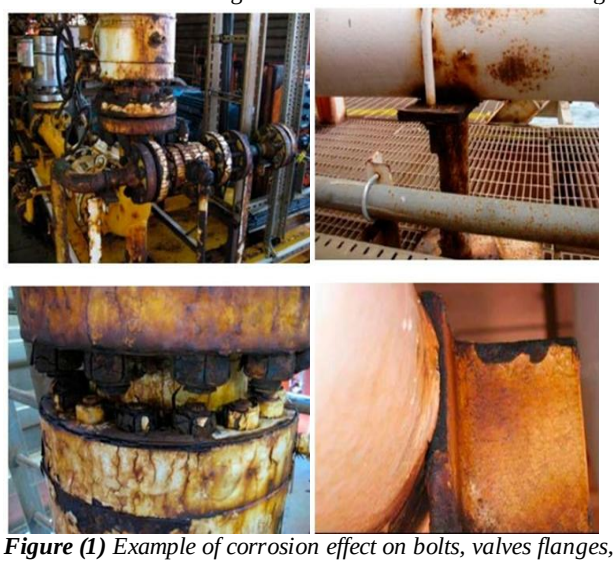


Figure (1) *Example of corrosion effect on bolts, valves flanges, piping, and pipe support (Abdeen, et al., 2019).*

Corrosion and Nano-materials: The field of nanomaterial have found one of the most promising topics in different applications such as chemistry, engineering, physics, biology that will change the direction of nanotechnology advances in wide range of fields. The term "nano-materials" employed to describe of the creation and exploitation the materials where at least one dimension in the range from approximately 1-100 nanometer. Due to their unique properties in nanoscale, observations showed that nanomaterial's are different from their bulk moieties and cannot be studied as same as from their bulk molecules [13]. The use of nano-materials reduces the content of costly and toxic elements in alloy components, which gives high profitability in material cost, excellent performance, and enhances the mechanical properties of the coating. Electro-deposition and sol-gel chemistry method are attractive techniques in Nano-coatings applications, as it is cheaper and novel strategies [14,15]. Nano coatings have significant potentials to resistance the corrosion performance of surfaces compared to micro material coatings. Due to their fine grain sizes, nano-crystal line structures are superior over microstructures for corrosion resistance .where provide a better filling ,a higher integrity of the coated surface and it also called for the availability

of chromium-toxic coating replacements . However, the coating thickness and composition should optimize to avoid decrease its protective characteristics towards corrosive and eroding influences [16]. Corrosion induces changes in the composition of the elements and decreases in grain size, contributing to the deterioration of corroded materials' mechanical properties (yield strength, ultimate strength, and failure strain). Applied stress accelerates corrosion and the loss of ultimate strength and failure strain of corroded materials exacerbated by its interaction with corrosion [17]. Anti-corrosion nano-materials and their coatings play an important role in improving mechanical properties such as linear stresses, ductility, high hardness, etc. in addition to surface properties such as residual stresses, surface roughness and distribution of particles on surface [18].

Research Objectives:
The main objective of this part is to study and analyze the linearized stresses improvement and their effect on corrosion resistance due to the application of nano coating of pressurized carbon steel pipe by Cobalt and Zinc nano-particles separately of thickness of 300, 600, 900 μm and 10 micrometer [3].

Research Methodology: A comprehensive review of the literature pertaining to nano- materials and their applications in the field of corrosion has undertaken in order to achieve the above objectives for this research. Then a group of nano-material's with corrosion-resistant properties will be selected and simulated the effect of apply nano coating technology using ANSYS software on a thick-walled cylindrical pipe that carries salty water under internal pressure, using electro-deposition nano coating method. After that will study and analyze the results and compare the changes in linearized stresses and in corrosion mechanical properties before and after applying coating by nano-materials of different thickness.

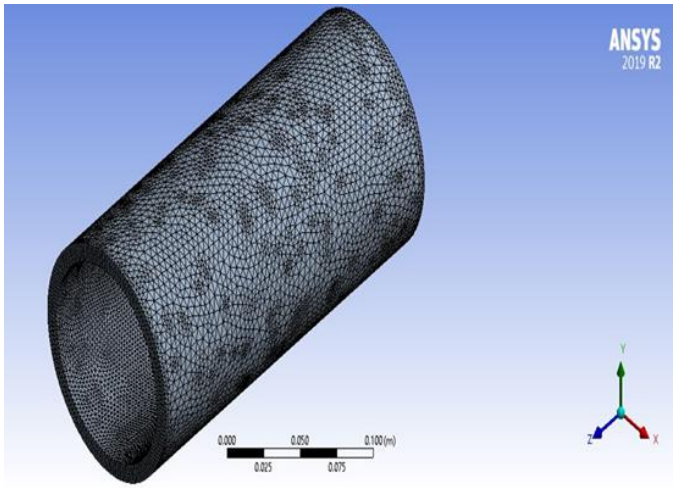


Figure (2) *Thick-walled cylindrical pipe with 4.5 mm on outer and side faces and 3.5 mm on inner face elements size of mish.*

The geometric modeling of the study: One finite element model has created. Thick walled cylindrical pipe coated with different nano thickness of Zinc and Cobalt materials separately, as in figures (2 to 5), which show the pipe specimen will analyze and coated during this work. At the beginning, the CAD geometry built using space claim in ANSYS with the given dimensions. Geometry transferred into ANSYS mechanical and thin nano layer defined on the inner surface wall using surface coating from ANSYS, [3,4].

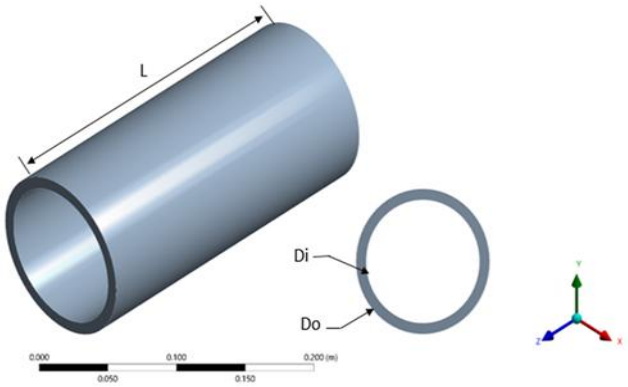


Figure (3) *Front and ISO views of thick-walled cylindrical pipe specimen with dimensions.*
Where:
L= 0.25m Do = 0.1143 m Di = 0.0971804 m

Mesh Details: Parts was converted to small elements in order to use FEA methods for solving the problem, refinement of mesh was done on the inner wall where the nano coating is located in order to get more accurate results, number of nodes is 143620 and elements is 71929 [3,4], as in figure-2

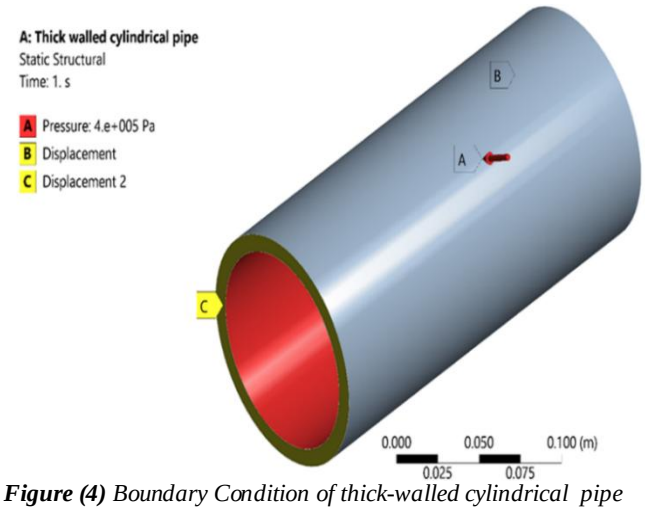


Figure (4) *Boundary Condition of thick-walled cylindrical pipe specimen.*

Materials: In the present work cobalt and zinc which are anticorrosion nano-material's will be used to apply coating on a thick-cylindrical pipe made from carbon steel, the physical, chemical and mechanical properties of the materials will be analysis before and after coating by nano-materials [4].

Carbon Steel: Carbon steels defined as those containing iron, carbon, and manganese. There are three type of carbon steel depend on the amount of carbon content is low carbon, medium carbon, and high carbon steel which contains 0.6–1.4% carbon. (Pressure System Design. 2012). It is the most widely used engineering material for service in seawater and many engineering applications in high temperature conditions such as power plant, chemical treatment, mining, mineral equipment Processing and other industrial fields, it offers many advantages of low price, easy availability, ease of fabrication, and a satisfactory rate of corrosion [19, 20, 21]. Carbon steel piping and tubing because of their

minimal resistance to corrosion there are limits on their operating time [22].

Zinc: Zinc is the fourth most used engineering metal in the world, a bluish-white metal, and one of the main uses for zinc is steel coating to protect against corrosion in the presence of an electrolyte such as moist soils or seawater [23].

Cobalt: Cobalt is one of the rare elements in the Earth's crust of about 0.1%, usually distributed in conjunction with nickel, lead, silver, iron, etc. It is a white, hard-bluish, ferromagnetic metal, relatively unreactive and slowly dissolves in mineral acids without union with hydrogen or nitrogen. Cobalt is now widely used in the production of alloy steel, which is the base metal in most of them. Cobalt alloys distinguished by being strength, high melting point, and high resistance to oxidation [24, 25].

Linearized Normal Stress: Stress linearization is the separation of stresses through a section into constant membrane. Linear bending stresses and total stress along a straight-line path, the linearized normal stress in (Y-axis) value and improvement represented in figures (5 to 10) and tables (1 to 4). Stresses along the thickness calculated through membrane stress for shell in the transverse direction, the longitudinal direction, and in plane shear. This theory applied only when shell bodies and solids that meshed with shell element. When highly localized stress occurs at a discontinuity in the load stress theory can apply. Most common example of peak stress when highly stress values on sharp edges as in figure-5 [3, 4, 5].

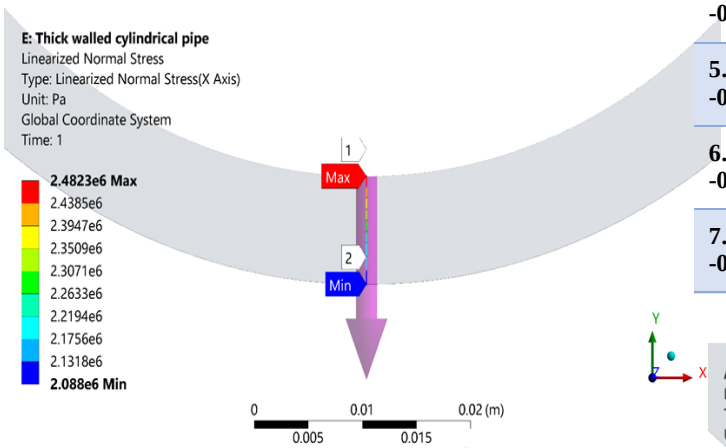


Figure (5) *Linearized Normal Stress (Y-axis) of Carbon steel (ASTM A53) pipe without coating*

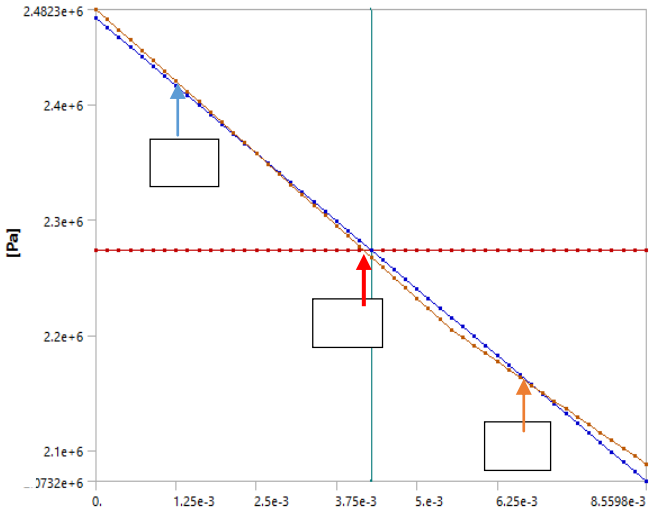


Figure (6) (a) *Membrane [Pa], (b) Membrane +Bending [Pa], (c) Total stress [Pa] without coating.*

Table (1) *Linearized normal stresses of carbon steel pipe without coating*

Length [m]	Membrane [Pa]	Bending [Pa]	Membrane +Bending [Pa]	Peak [Pa]	Total [Pa]
0.0000E+00	2.27E+06	2.0066E+05	2.4745E+06	7.8158E+03	2.4823E+06
1.7833E-04		1.9230E+05	2.4662E+06	7.2620E+03	2.4734E+06
3.5666E-04		1.8394E+05	2.4578E+06	6.7081E+03	2.4645E+06
5.3499E-04		1.7558E+05	2.4494E+06	6.1543E+03	2.4556E+06
7.1332E-04		1.6722E+05	2.4411E+06	5.6004E+03	2.4467E+06
8.9165E-04		1.5886E+05	2.4327E+06	5.0466E+03	2.4378E+06
1.0700E-03		1.5050E+05	2.4244E+06	4.4927E+03	2.4289E+06
2.1400E-03		1.0033E+05	2.3742E+06	1.1697E+03	2.3754E+06
3.0316E-03		5.8527E+04	2.3324E+06	-2.0267E+03	2.3304E+06
4.1016E-03		8.3610E+03	2.2822E+06	-5.5006E+03	2.2767E+06
5.1715E-03		-4.1805E+04	2.2321E+06	-8.9744E+03	2.2231E+06
6.0632E-03		-8.3610E+04	2.1903E+06	-6.3741E+03	2.1839E+06
7.1332E-03		-1.3378E+05	2.1401E+06	2.7006E+03	2.1428E+06

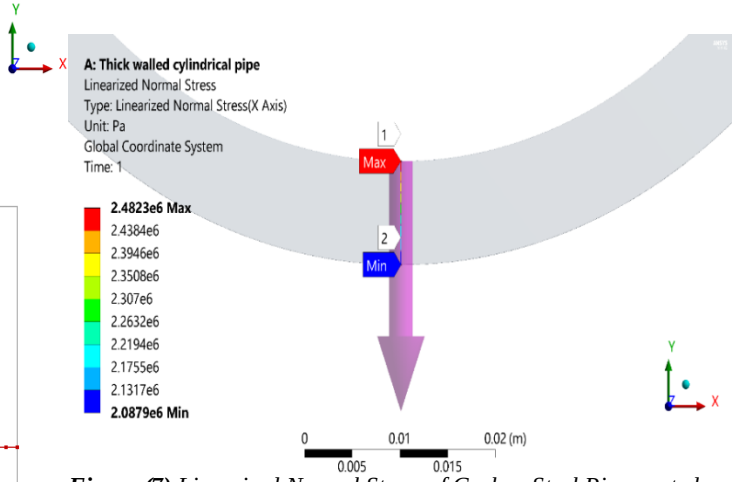


Figure (7) *Linearized Normal Stress of Carbon Steel Pipe coated with 300 Nanometer of Cobalt*

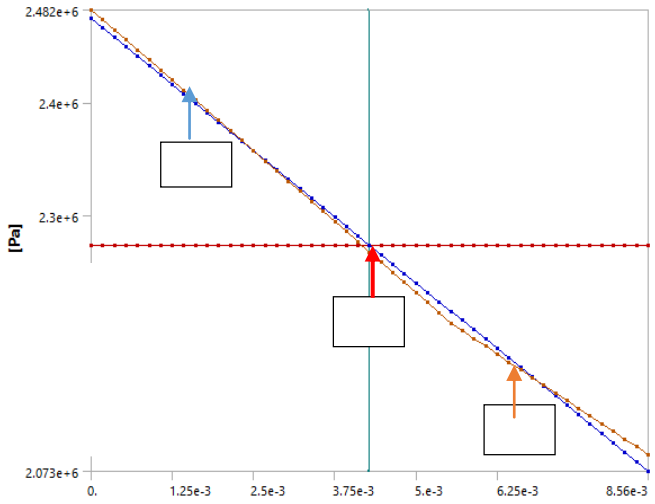


Figure (8) (a) *Membrane [Pa], (b) Membrane +Bending [Pa], (c) Total stress [Pa] coated with 300 Nanometer of Cobalt*

Table (2) *Linearized normal stresses of Carbon Steel Pipe coated with 300 Nanometer of cobalt*

Length [m]	Membrane [Pa]	Bending [Pa]	Membrane +Bending [Pa]	Peak [Pa]	Total [Pa]
0.00000 E+00	2.27E+06	2.00660 E+05	2.47440 E+06	7.81530 E+03	2.48230 E+06
1.78340 E-04		1.92300 E+05	2.46610 E+06	7.26150 E+03	2.47330 E+06
3.56670 E-04		1.83940 E+05	2.45770 E+06	6.70770 E+03	2.46440 E+06
5.35010 E-04		1.75580 E+05	2.44940 E+06	6.15390 E+03	2.45550 E+06
7.13340 E-04		1.67220 E+05	2.44100 E+06	5.60010 E+03	2.44660 E+06
8.91680 E-04		1.58860 E+05	2.43260 E+06	5.04630 E+03	2.43770 E+06
1.07000 E-03		1.50500 E+05	2.42430 E+06	4.49250 E+03	2.42880 E+06
2.14000 E-03		1.00330 E+05	2.37410 E+06	1.16970 E+03	2.37530 E+06
3.03170 E-03		5.85270 E+04	2.33230 E+06	-2.02650 E+03	2.33030 E+06
4.10170 E-03		8.36100 E+03	2.28210 E+06	-5.50010 E+03	2.27660 E+06
5.17170 E-03		-4.18050 E+04	2.23200 E+06	-8.97370 E+03	2.22300 E+06
6.06340 E-03		-8.36100 E+04	2.19020 E+06	-6.37440 E+03	2.18380 E+06
7.13340 E-03		-1.33780 E+05	2.14000 E+06	2.70030 E+03	2.14270 E+06
8.02510 E-03		-1.75580 E+05	2.09820 E+06	1.03010 E+04	2.10850 E+06

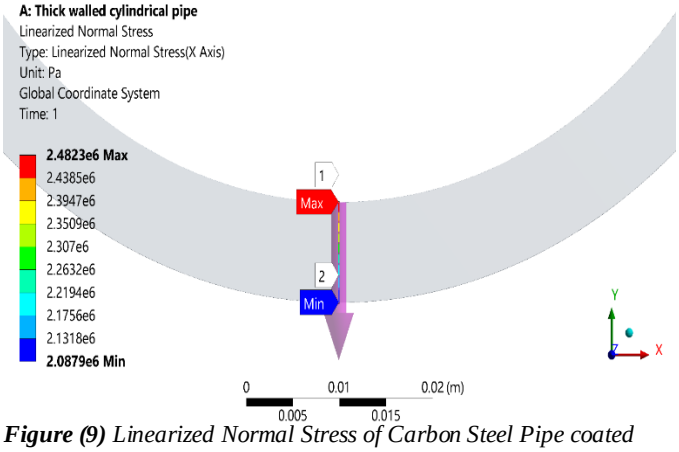


Figure (9) *Linearized Normal Stress of Carbon Steel Pipe coated with 300 Nanometer of Zinc*

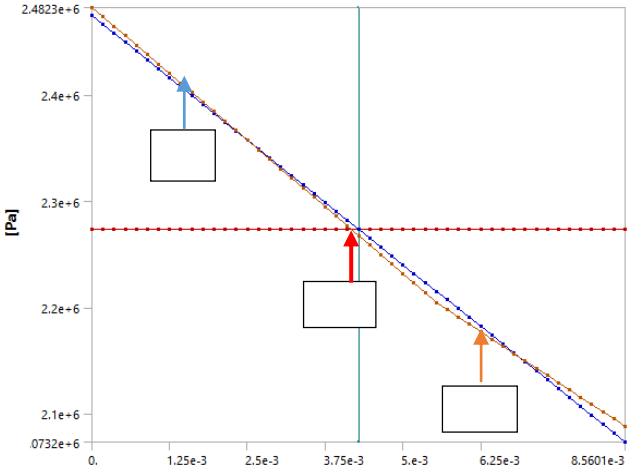


Figure (10) *(a) Membrane [Pa], (b) Membrane +Bending [Pa], (c) Total stress [Pa] coated with 300 Nanometer of zinc*

Table (3) *Linearized normal stress values of Carbon Steel Pipe coated with 300 nanometer of zinc*

Length [m]	Membrane [Pa]	Bending [Pa]	Membrane +Bending [Pa]	Peak [Pa]	Total [Pa]
0.00000 E+00	2.27E+06	2.00670 E+05	2.47450 E+06	7.81550 E+03	2.48230 E+06
1.78340 E-04		1.92310 E+05	2.46610 E+06	7.26170 E+03	2.47340 E+06
3.56670 E-04		1.83950 E+05	2.45780 E+06	6.70790 E+03	2.46450 E+06
5.35010 E-04		1.75590 E+05	2.44940 E+06	6.15410 E+03	2.45560 E+06
7.13340 E-04		1.67220 E+05	2.44110 E+06	5.60020 E+03	2.44670 E+06
8.91680 E-04		1.58860 E+05	2.43270 E+06	5.04640 E+03	2.43770 E+06
1.07000 E-03		1.50500 E+05	2.42430 E+06	4.49260 E+03	2.42880 E+06
2.14000 E-03		1.00330 E+05	2.37420 E+06	1.16970 E+03	2.37530 E+06
3.03170 E-03		5.85280 E+04	2.33240 E+06	-2.02650 E+03	2.33030 E+06
4.10170 E-03		8.36120 E+03	2.28220 E+06	-5.50020 E+03	2.27670 E+06
5.17170		-	2.23200	-	2.22310

E-03		4.18060 E+04	E+06	8.97390 E+03	E+06
6.06340 E-03		-8.36120 E+04	2.19020 E+06	-6.37460 E+03	2.18380 E+06
7.13340 E-03		-1.33780 E+05	2.14010 E+06	2.70040 E+03	2.14280 E+06
8.02510 E-03		-1.75590 E+05	2.09820 E+06	1.03010 E+04	2.10850 E+06

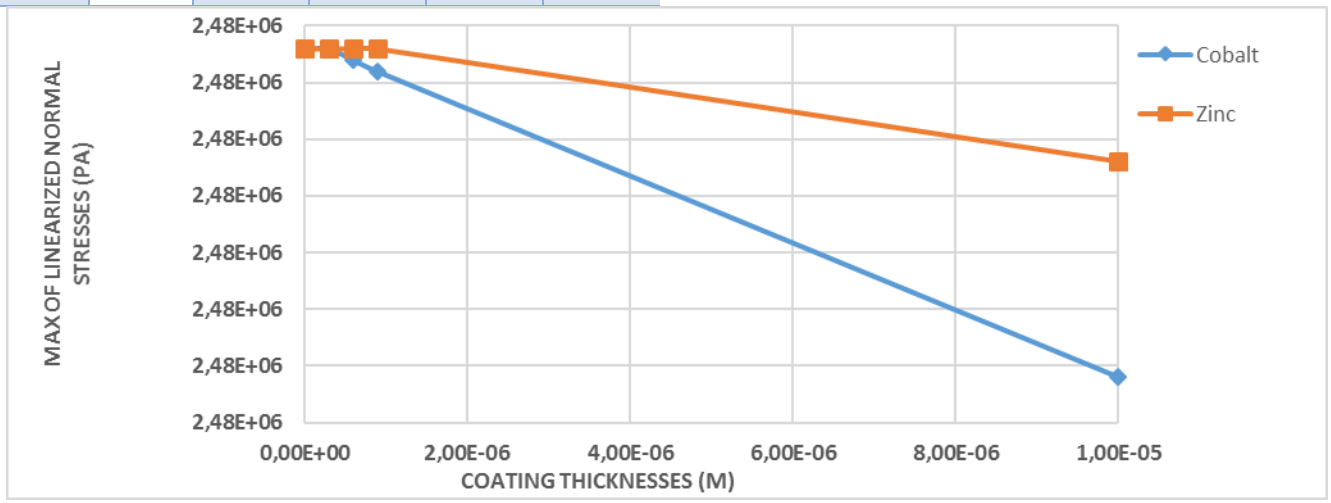


Figure (11) *Comparison of maximum Linearized Normal Stress (Y-axis) With Cobalt and Zinc of different nano coating thicknesses.*

Table (4) *Maximum Linearized Normal Stress value and percentage of improvement in corrosion resistance with different coating thickness (Y-axis).*

	Cobalt(Co)			Zinc(Zn)		
Coating thickness (m)	**Value (Pa)**	**Improvement %**	**Corrosion Resistance %**	**Value (Pa)**	**Improvement %**	**Corrosion Resistance %**
0	**2.48230E+06**	**0**	**0**	**2.48230E+06**	**0**	**0**
300 *nm*	**2.48230E+06**	**0**	**0**	**2.48230E+06**	**0**	**0**
600 *nm*	**2.48220E+06**	**0.004028522**	**0.635**	**2.48230E+06**	**0**	**0**
900 *nm*	**2.48210E+06**	**0.008057044**	**0.898**	**2.48230E+06**	**0**	**0**
10 *μm*	**2.47940E+06**	**0.116827136**	**3.418**	**2.48130E+06**	**0.040285219**	**2.007**

Results Discussion: Figure (11) shows a comparison of maximum linearized normal stresses (Y-axis) of a pressurized carbon steel (ASTM A53) thick-walled cylindrical pipe and the improvement due to coating with different nano thicknesses of Cobalt and Zinc separately. Starting with thickness (300, 600, 900 nanometers to 10 micrometer). It is clear that the linearized normal stress (Y-axis) did not change when coated with 300 nanometer for both coating materials, but it began to decrease slightly when coated with 600 nanometer of Zinc and fast decreasing with 10 microns. While, when coated with 600 and 900 Cobalt, can be noticed that there is a noticeable decrease on linearized normal stresses and become more sharply decreasing when the coating was 10 microns. The maximum improvement is (0.1168%) when coated with 10 µm of cobalt, which is (34. %) higher than zinc. The same behavior was found in the resistance of corrosion where the increase started at 600 µm of cobalt with value (0.635%) and it reached the highest value (3.418%).While coating by zinc nanoparticle at (10 mm) found to be (2.007%).

Conclusions: From the analysis of the above results, the following main points can extracted:

- The Carbon steel (ASTM A53) thick walled cylindrical pipe subjected to internal pressure was successfully coated theoretically with anticorrosion nano- particles of Cobalt and Zinc using ANSYS software (version.19 with different nano thicknesses of 300 µm, 600 µm, 900 µm and 10 µm separately.
- Coating with 300 nanometers of both Znic and Cobalt nano-particles, the linearized normal stresses (Y-axis) did not change but starts to decrease slightly when coated with 600 nanometers of cobalt and continues to decrease with 10 µm with greater than zinc. On the other hand, when coated with 600-µm and 900-µm zinc, it noticed that there is no difference in the linearized normal stresses.
- The value of improvement in the rate of corrosion resistance began to increase when coating with 600 µm of cobalt until became (3.418%).
- The overall improvement in linearized normal stresses and corrosion resistance due to cobalt coating can be about (66 %) higher in comparison with Zinc at 10 µm thickness of coating.
- Cobalt nano-coating has shown to be a promising technique to improve corrosion and linearized stresses resistance.

References:

[1] Abdeen, D., El Hachach, M., Koc, M., & Atieh, M. (2019). A Review on the Corrosion Behavior of Nano coatings on Metallic Substrates. Materials, 12(2)

[2] ASTM A53 / A53M-18, Standard Specification for Pipe, Steel, ~~Black and~~ Hot-Dipped, Zinc-Coated, Welded and Seamless, ASTM International, West Conshohocken, PA, 2018, www.astm.org).

[3] Al-Juboori, S., Albtoosh, M., 2019. Improving the Mechanical Properties of Conventional Materials by Nano-coating, part-1. V International Scientific Conference Marerial Science „Nonequilibrium Phase Transformations", Varna, Bulgaria.

[4] Al-Juboori, S., Albtoosh, M., 2019Improving the Linearized stresses resistance by Nano-Coating, Part-2 Proceeding of International Scientific Conference High Technologies. Business. Society09-11.03.2020, Borovets, Bulgaria, Year V, Issue 2 (8), Sofia, Bulgaria 2020

[5] Al-Juboori S. and Dana Alshamaileh, Improving the Corrosion Resistance by nano-Materials Coating, part-1, v international scientific conference material science no equilibrium phase transformations 09 - 12 September 2019, Varna, Bulgaria

[6] Beyene, F. (2016). A Review on nano-coating of Metallic Structures to Improve Hardness and Maintaining Toughness. I-manager's Journal on Material Science, 4(1), 32-40.

[7] Cosham, A., Hopkins, P., & Macdonald, K. (2007). Best practice for the assessment of defects in pipelines – Corrosion. Engineering Failure Analysis, 14(7), 1245–1265.

[8] CRC Handbook of Chemistry and Physics, Robert C. Weast, Ed. 62 Edition, Crc Press, Boca Raton, FL,1981. http://www.matweb.com/index.aspx

[9] Darvell, B. (2018). Corrosion. Materials Science for Dentistry, 382–398.Dhoke, S. Khanna, A. & Sinha, T. (2009). "Effect of nano-ZnO particles on the corrosion behavior of alkyd-based waterborne coatings." Progress in Organic Coatings, 64(4), 371–382.

[10] Farag, A. (2020). Applications of nanomaterials in corrosion protection coatings and inhibitors. Corrosion Reviews.

[11] Ferreira, M. Zheludkevich, M. & Tedim, J. (2011). Advanced protective coatings for aeronautical applications. Nanocoatings and Ultra-Thin Films, 235–279.

[12] Jose, R., Sakho, E. hadji M., Parani, S., Thomas, S., Oluwafemi, O. S., & Wu, J. (2019). Introduction to nanomaterials: synthesis and applications. Nanomaterials for Solar Cell Applications, 75–95.

[13] HEARN, E. (1997). THICK CYLINDERS. Mechanics of Materials 1, 215–253.

[14] Hou, Y., Lei, D., Li, S., Yang, W., & Li, C.-Q. (2016). Experimental Investigation on Corrosion Effect on Mechanical Properties of Buried Metal Pipes. International Journal of Corrosion, 2016, 1–13.

[15] Gao, Y., Ward, L., Fan, L., Li, H., & Liu, Z. (2019). A study of the use of polyaspartic acid derivative composite for the corrosion inhibition of carbon steel in a seawater environment. Journal of Molecular Liquids, 111634.

[16] Klarstrom, D., & Crook, P. (2001). Cobalt Alloys: Properties and Applications. Encyclopedia of Materials: Science and Technology, 1281–1288.

[17] Khodair, Z. Khadom, A. & Jasim, H. (2018). Corrosion protection of mild steel in different aqueous media via epoxy/nanomaterial coating: preparation, characterization and mathematical views. Journal of Materials Research and Technology.

[18] Lynch, R. (2001). Zinc: Alloying, Thermomechanical Processing, Properties, and Applications. Encyclopedia of Materials: Science and Technology, 9869–9883.

[19] Li, L., Li, C.-Q., & Mahmoodian, M. (2019). Effect of Applied Stress on Corrosion and Mechanical Properties of Mild Steel. Journal of Materials in Civil Engineering, 31(2), 04018375.

[20] Mutahhar, F., Aithan, G., Iski, E. V., Keller, M. W., Shirazi, S., & P. Roberts, K. (2017). Mechanistic modeling of erosion–corrosion for carbon steel. Trends in Oil and Gas Corrosion Research and Technologies, 749–763.

[21] Nguyen Tri, Nguyen, T. Rtimi, S., & Ouellet Plamondon, C. (2019). Nanomaterials-based coatings: an introduction. Nanomaterials-Based Coatings, 1–7.

[22] Païdoussis, M. (2016). Cylindrical Shells Containing or Immersed in Flow. Fluid-Structure Interactions, 1–141.
Pressure System Design. (2012). Lees' Loss Prevention in the Process Industries, 509–617.

[23] Qu, Z., Wang, L., Tang, H., Ye, H., & Li, M. (2019). Effect of Nano-SnS and Nano-MoS2 on the Corrosion Protection Performance of the Polyvinylbutyral and Zinc-Rich Polyvinylbutyral Coatings. Nanomaterials, 9(7), 956.

[24] Solatani, H., Tavoosi, M., & Loghman-Estarki, M. R. (2019). Fe-Ni composite coatings reinforced with SiC nanoparticles and carbon nanotubes: corrosion and tribological performance. Materials Research Express.

[25] Sankara, T. (2012). Nanocoatings to improve the tribocorrosion performance of materials. Corrosion Protection and Control Using Nanomaterials, 167–212.

Impostation of an experimental design for studying the optimization of artificial aging process for the aluminium alloys

Irida Markja
Faculty of Mechanical Engineering, Polytechnic University of Tirana, Albania
*imarkja@fim.edu.al ; irida.markja@gmail.com

Abstract: *New area industry of Albania, in recent years, factories with closed cycle of production and processing of aluminium alloys are being targeted. In Albania about 25,000 tons of aluminum alloys per year are produced and there is a tendency to increase this production. This reality has encouraged us to undertake a number of studies with the primary objective for optimizing the parameters of the basic process of this industry. In this article we focus on the process of artificially aging aluminum alloys. From early and newer studies [2], the importance and delicacy of temperature-time parameters in the evolution of microstructure and in the mechanical properties of the final product are recognized and underlined. We have impost an experimental planning based on the Response Surface Method by choosing Central Composite Design to optimize the temperature and time parameters for the artificial aging with the objective of maximizing the process indicator - mechanical properties, hardness in our case. The plan includes 13 tests with 5 replicas in the center of the experiment, built with the help of Design-Expert DX7 and DX13 software. The focus of our attention was the assesment of the design, analysis of residuals and diagnostic diagrams and forms of presentation of results: mathematical model, 3D response surface, isocontours and* effects *of interaction between factors. In the future works we will present the experimental results of the optimization of the artificial aging process for different aluminium alloys produced in Albania.*
Keywords*: RSM, CCD, ALUMINIUM ALLOY, AGING, OPTIMIZATION, DESING EXPERT*

1. Introduction

On the production and processing industry of aluminum in Albania

Starting from the 90s and especially after the 2000s in Albania, many factories and companies have been set up with the main object of processing aluminum and its alloys, mainly for the production of aluminum profiles. Today there are several dozen of them. Some of the largest companies have included in their production scheme the foundry line for the production of aluminum alloys based on recycled materials. Each of these companies produces from the foundry approximately five thousand tons per year. The aluminum produced is processed almost entirely in the country. To respond to the challenges of meeting the ever-increasing demands of quality products as most of them are mainly destined for export to developed countries. This industry is turning its attention to the university unlike what happened before. To respond to this new industrial reality we have planned and are undertaking a series of researches starting with the optimization of the parameters of artificial aging of aluminum alloys.

On the importance of the process of artificial aging of aluminum alloys

The industry of production and processing of aluminum alloys in Albania is in the early stages of its development and as such feels the need for studies in support of it and especially for the optimization of key processes. One of the processes that gives the impront to the mechanical properties of products made of aluminum alloys is that of artificial aging, as the final process of thermal processing. From earlier, but also newer studies, the importance and delicacy of artificial aging of aluminum alloys is recognized and underlined. Indeed, it is a process of strengthing oo the alloys by managing the transformation of a supersatureted solid solution. During this process, the formation and growth of precipitate particles of the second phases from the supersaturated solid solution occurs. It is a process that is controlled by the diffusion of atoms of dissolved elements and as such significantly influenced by the parameters of the process temperature and time, for a given chemical composition of the alloys and a optimized homogenization annealing. The characteristics of precipitated particles depend on the temperature and time parameters of artificial aging: size, distribution, relative quantities which determine the degree of strengthening of the alloy. Precisely for these reasons, we are undertaking a series of studies to optimize the parameters of the artificial aging process of aluminum alloys produced in Albania with the objective of maximizing mechanical properties, starting from hardness.

2.Choosing the Experiment Plan

Among the plans that offer optimization of the indicators we have chosen the Response Surface Method - **RSM**, and Central Composite Design - **CCD**. The CCD plan offers more experiment points compared to the simple factorial plan, while maintaining a minimum total number of tests. The CCD plane also offers the rotary property, which means that the same error is stored at a certain distance from the center of the experiment. The response surface method, as an optimization method, was developed in the 1950s and was first applied in the process industries (chemical, metallurgical, etc.). This method constitutes the optimization technique based on the programming of the most widespread and successful experiments even today. [5] Our e experimental plan was draft on recent industrial development in which was applied this experimental plan and also on the latest articles, scientific research regarding the experimental plan. [6]

3. Impostation of our CCD experimental plan

The primary objective of this study is to optimize the process of artificial aging of aluminum alloys, in order to maximize the mechanical properties, strength, tensile strength, hardness. For the construction of the plan we have chosen as the center of the experiment the value of the process parameters, temperature and aging time, approximate to the values applied by the manufacturers for some aluminum alloys: temperature T = 185 ^{o}C, time t = 8h. As a step value for these two parameters we have chosen: $\Delta T = 15\ ^{o}C$, $\Delta t = 3h$. These step values provide approximately the same change / effect on the process indicator (hardness), considered different bibliographic sources (Fig.1).

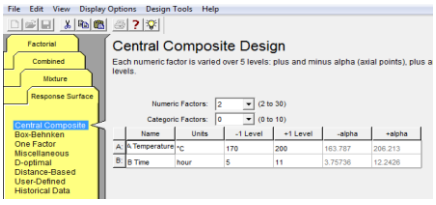


Fig.1 *From application to software for imposting the experiment plan*

For the star points arm, based on the recommendation in the Desing Expert tutorial, we have accepted the value +/- √2 (α = +/- 1.4214).

By entering this data, for *Factor A - Temperature* and *Factor B - Time*, in the software Design - Expert (RSM Method, CCD Plan), we obtain the Experimental Plan Table (Tab.1). In the experimental plan table are presented according to the factor combination and according to the order of the performing tests: *run*.

Table 1: *Experimental plan table for the experiment*

	Std	Run	Block	Factor 1 A: Temperature °C	Factor 2 B: Time h	Response 1 Hardness HBN
	5	1	Block 1	163.7867966	8	
	4	2	Block 1	200	11	
	1	3	Block 1	170	5	
	7	4	Block 1	185	3.757359313	
	8	5	Block 1	185	12.24264069	
	13	6	Block 1	185	8	
	3	7	Block 1	170	11	
	6	8	Block 1	206.2132034	8	
	12	9	Block 1	185	8	
	10	10	Block 1	185	8	
	11	11	Block 1	185	8	
	2	12	Block 1	200	5	
	9	13	Block 1	185	8	

In the experimental plan table all the tests are presented according to the combination of factors as well as according to the order of performing the tests (run). To demonstrate the method, we have obtained, for the indicator *"hardness-HRB"*, approximate results from various bibliographic sources and our unpublished works.

4. Analysis of Variance, ANOVA

The result of the analysis of variance (ANOVA) processed by the software is given in the following table (Tab.2)

Table 2: *Anova for response surfare quadratic model*

Transform | Fit Summary | Model | ANOVA | Diagnostics | Model Graphs

Use your mouse to right click on individual cells for definitions.

Response 1 Hardness

ANOVA for Response Surface Quadratic Model

Analysis of variance table [Partial sum of squares - Type III]

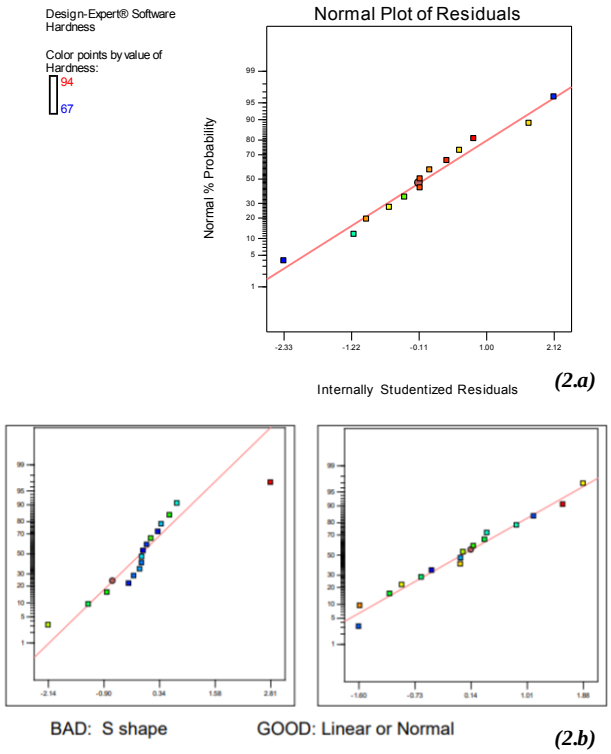
Source	Sum of Squares	df	Mean Square	F Value	p-value Prob > F	
Model	967.41	5	193.48	30.17	0.0001	significant
A-A Temperatur	*101.93*	*1*	*101.93*	*15.89*	*0.0053*	
B-B Time	*272.59*	*1*	*272.59*	*42.50*	*0.0003*	
AB	*182.25*	*1*	*182.25*	*28.41*	*0.0011*	
A²	*151.23*	*1*	*151.23*	*23.58*	*0.0018*	
B²	*308.79*	*1*	*308.79*	*48.14*	*0.0002*	
Residual	44.90	7	6.41			
Lack of Fit	*36.10*	*3*	*12.03*	*5.47*	*0.0671*	*not significant*
Pure Error	*8.80*	*4*	*2.20*			
Cor Total	1012.31	12				

Interpretation of ANOVA table for our ezperimental data: The Model F-value of 30.17 implies the model is significant. There is only a 0.01% chance that a "Model F-Value" this large could occur due to noise. Values of "Prob > F" less than 0.0500 indicate model terms are significant. In this case A, B, AB, A2, B2 are significant model terms. Values greater than 0.1000 indicate the model terms are not significant. If there are many insignificant model terms (not counting those required to support hierarchy), model reduction may improve your model. The "Lack of Fit F-value" of 5.47 implies there is a 6.71% chance that a "Lack of Fit F-value" this large could occur due to noise. [1,2,3]

5. Analysis of residuals and diagnostic diagrams

Before we can see and evaluate the results, we have to verify/diagnose the model. The assumptions and assertions made in the theory of Analysis of Variance must be fulfilled by the results of the experiment. As an illustrative example, we bring one of the assumptions made, that regarding to the "normality of the random size of residuals". For this, in the following we are bringing, the dependence on our experiment as well as two versions of this behavior (when not fulfilled and when the assumption is fulfilled) offered by the tutorial of Design - Expert 7 and 13.

5.1 Normal probability plot of the studentized residuals to check for normality of residuals.



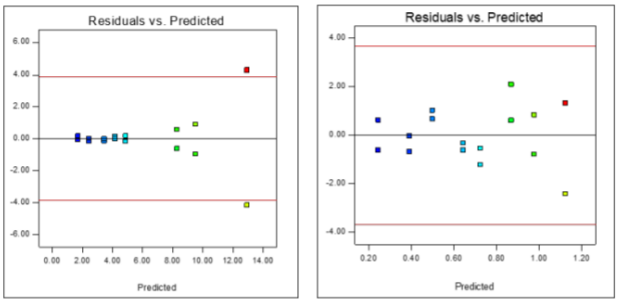
(2.a) ***(2.b)***

Fig. 2 *Normal Plot of residuals a) from our experiment b) from the DX software*

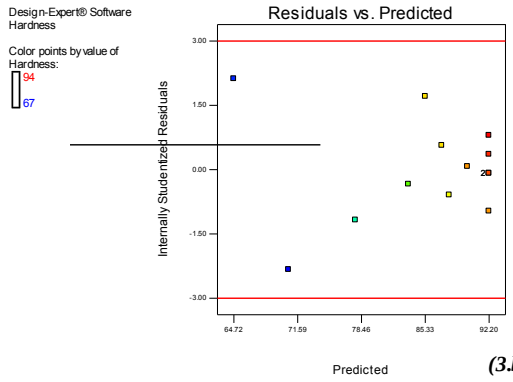
If the test points are placed in the form of an "S" the normality is not met (Fig. 2.b on the left) and when they are placed by random distribution around a straight line, the normality is met (Fig 2.b on the right). By carefully observing the graphs (Fig. 2a) it is concluded that in our experiment the assumption on the Normality of the random size of the residuals is fulfilled.

In the following we are bringing the diagnostic graphs for two other assumptions for which the same reasoning logic is followed also the graph for the power of transformation.

5.2 Studentized residuals versus predicted values to check for constant error.



(3.a)

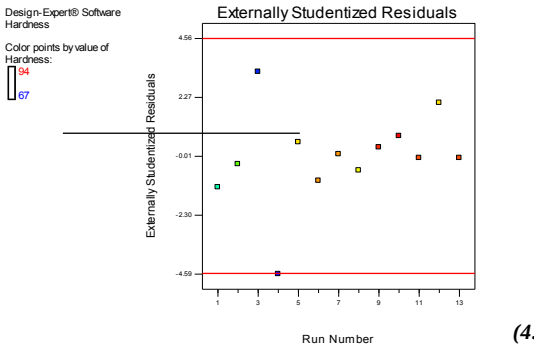


(3.b)

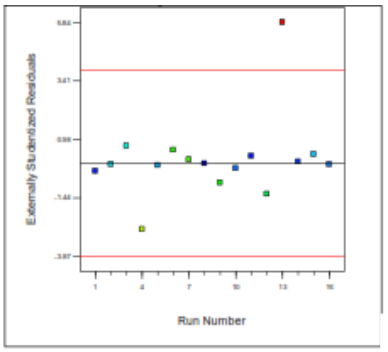
Fig. 3 *Residuals vs Predicted a) from the DX software b) from our experiment*

If the test points are distributed randomly, within the limit limits, the assumption is met and if the distribution gains certain geometry (megaphone in this case) the assumption is not met (Fig. 3.a). By carefully observing the graphs it is concluded that in our experiment the assumption on constant error is fulfilled (Fig. 3.b).

5.3 Externally Studentized Residuals to look for outliers, i.e., influential values.



(4.a)

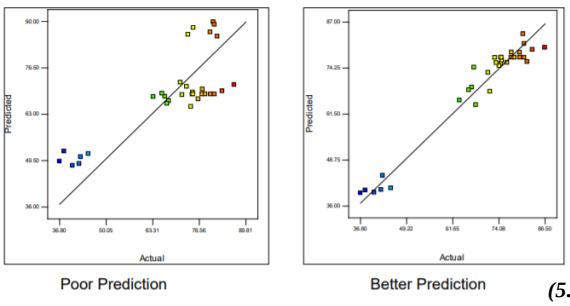


(4.b)

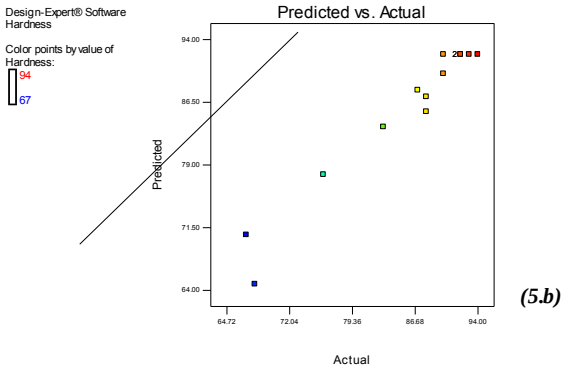
Fig. 4 *Externally Studentized Residuals vs Run : a) from our experiment b) from the DX software*

By carefully observing the graphs it is concluded that in our experiment the assumption on the affected values is fulfilled, we have no evidence points outside the limits (Fig.4.a).

5.4 Predicted vs. Actual



(5.a)

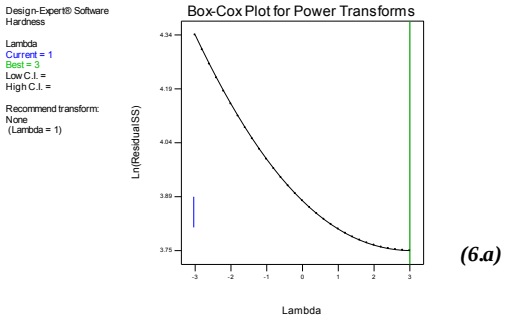


(5.b)

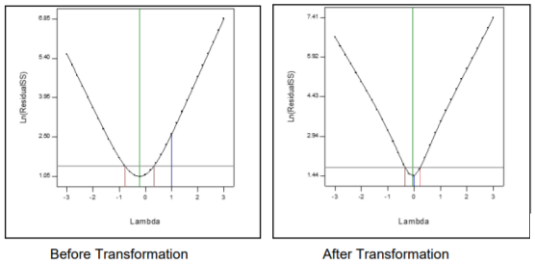
Fig. 5 *Predicted vs. Actual: a) from the DX software b) from our experiment*

The test points should be randomly distributed around the straight line at an angle of 45°, if clusters of points above or below the straight line are observed this indicates high or poor predictability (Fig. 5.a). By carefully observing the graphs it is concluded that in the experiment the predictability from the mathematical model is satisfactory (Fig. 5.b).

5.5 Box-Cox plot for power transformations.



(6.a)



(6.b)

Fig. 6 *Box-Cox plot for power transformations a) from our experiment b) from the DX software*

When the ratio $y_{max}/y_{min} > 10$ usually indicates a transformation is required. For raport $y_{max}/y_{min} < 3$ the power transforms have little effect (Fig.6.a).

By carefully observing our experiment (Fig.6.b) the ratio is 1.4099 that means it is not necessary the power transform: $y^{(\lambda=1)}$.

6. Results

Below we are shown the data generated from the DX software:

a. Mathematical model equations
b. Response Surface Method - RSM
c. Isocontours of the Indicator of Process (hardness, HBN)
d. Effects of interaction between factors (temperature-time)

a) Mathematical model equations for our experiment

Mathematical model equations: is a quadratic polynomial which expresses the process indicator (hardness HBN) depending from the factors and the interaction between them.

Final Equation in Terms of Coded Factors it is:

$$Hardness = +92.20 + 3.57 *A + 5.84*B - 6.75 *A*B - 4.66*A^2\ 6.66*B^2$$

Final Equation in Terms of Actual Factors it is:

$$Hardness = -945.98637 +9.10519* \text{ A Temperature } +41.54021*B \text{ Time } -0.15000* \text{ A Temperature } * \text{ B Time } -0.020722* \text{ A Temperature}^2 \ -0.74028* \text{ BTime}^2$$

b) Response surface method (RSM)

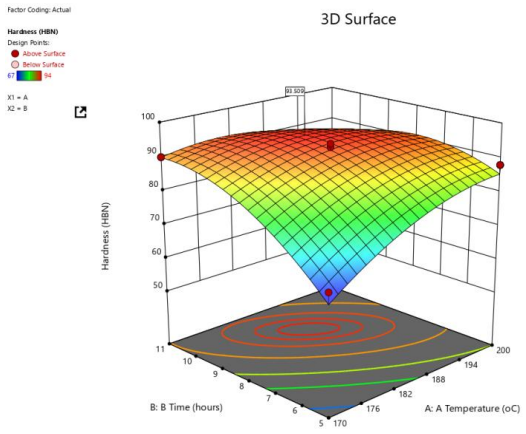


Fig. 7 *The response surface (3D) plot of Hardness vs Time-Temperature*

c) Isocontours of the Indicator of Process (hardness, HBN)

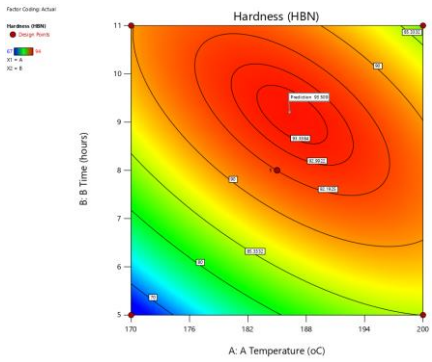


Fig. *The contour plot of Hardness (HBN) vs Time-Temperature*

d) Effects of interaction between factors *(temperature-time)*

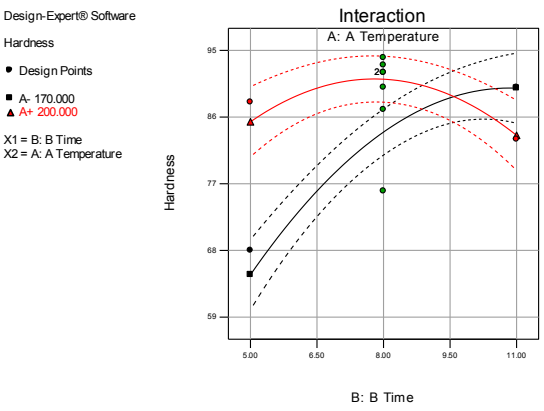


Fig. 9 *Interaction between factors*

7. Conclusions

1. In this paper we have presented the methodology for the planning and analysis of the experiment for the case RSM-CCD applied in artificial aging of aluminum alloys.
2. Careful planning of the experiment ensures that the results are obtained with the right expectation, within low probability errors (p-values), with a minimum number of tests.
3. The RSM-CCD method provides in addition to the 3D graphical representation of the response surface also:

- *Mathematical model* of the dependence of the process indicator on the factors taken in the study
- The *effect of the interaction between the factors* and what is more important:
- *Isocontours* of the indicator depending on the factors within the studied limits.
- We consider the latter especially important for industrial operators as it serves them as a ***technological card*** for process management.
- We hope that this paper will be useful for various researchers who aim to optimize the parameters of a process, as we are convinced that it will serve us in future work to optimize the parameters of artificial aging of various connections of aluminium.

8. Acknowledgment

The author gratefully acknowledges Polytechnic University of Tirana and Laboratory of Materials Science for supporting this research project; University of Lille France, for disponibility of software Design-Expert and Prof. Assoc. Dervish Elezi for professional advices.

9. Conflict of interests

The author would like to confirm that there is no conflict of interests associated with this publication and there is no financial fund for this work that can affect the research outcomes.

10. References

1. Handbook for Experimenters Version DX13.00 (2020)
2. https://www.statease.com
3. Manuale practico per realizzare, Disegni degli Esperimenti Version DX7
4. M.Kumar, M.M.Baloch, M.I.Abro, S.A.Memon; Effect of Artificial Aging Temperature on Mechanical Properties of 6061 Aluminum Alloy; Journal of Engineering and Technology, Vol.38,No.1, 31-36,; p-ISSN:0254-7821,E-issn:2413-7219 January (2019)
5. D.Elezi "Lecture-*Bases of process design*" Polytechnic University of Tirana; (2015)
6. Somsak Kaewploy, Chaiyoot Meengam "Determination of Optimal Parameters for Diffusion Bonding of Semi-Solid Casting Aluminium Alloy by Response Surface Methodology" MATEC 26, 02001 Web of Conferences ACMME pp.01-05 (2015)
7. P.Puspitasari , D.I. Tsamroh , M.Achyarsyah , B.Bandanajaya and D. Puspitasari; Multistage artificial aging optimization for tensile properties of Duralium using Response Surface Method (RSM); MATEC Web of Conferences 204, 00007 ; IMIEC (2018)
8. K.Dehgani, A.Nekahi, M.Mirzaie "Using response surface methodology to optimize the strain aging response of AA5052"MSE A527 ; 7442-7451 (2010)
9. M.Voncina, K.Kresnik, D.Volsak, J.Medved "Effects of homogenization of Aluminium Alloy EN AW 8006" Metals; (2020)
10. J.Hirsch "Annealing of Aluminium and Its Alloys; ASM Handbook, Vol 4E: Heat treating of nonferrous alloys, ASM International, Materials Park, pg.137-147, (2016)

Nanosized ZnO and ZnO@zeolite composite prepared via sonication method

Gospodinka Gicheva, Neli Mintcheva, Marinela Panayotova
University of Mining and Geology "St. Ivan Rilski", Sofia, Bulgaria
g.gicheva@mgu.bg

Abstract: *ZnO nanosized materials are well known for their photocatalytic and antibacterial properties. Their implication in water treatment and environmental protection, especially as a part of composite materials, has been an object of study of a great number of researchers working in the field. Zeolites are excellent candidates for support of composites preparation with semiconductor oxides since they are non-hazardous, non-expensive and naturally abundant materials. In order to synthesize nanosized ZnO with well-developed surface area and uniform size distribution in pristine form and supported on zeolite, we applied the method of precipitation assisted by sonication. As prepared ZnO nanoparticles and the composite ZnO-zeolite were characterized by XRD, SEM and UV-Vis spectroscopy. The ZnO crystalized in wurtzite structure in both materials. The morphology of ZnO nanoparticles was affected by the zeolite framework, as in the composite the ZnO was formed in-situ at the presence of zeolite. The ultrasonic irradiation during the precipitation of $Zn(OH)_2$ and aging of the reaction mixture causes activation of the zeolite surface and prevents the aggregation of ZnO particles. In result evenly distributed ZnO nanoparticles were obtained in the composite.*

Keywords*: ZnO NANOPARTICLES, SYNTHESIS, NANOCOMPOSITES, ZEOLITE*

1. Introduction

Zinc oxide (ZnO) is well-known and widely used material as an active ingredient in paints, plastic, cosmetics, medicine (common brand name(s): Aquaphor, Balmex, Medi-Paste, etc). It is a II-VI semiconductor with energy band gap of ~3.3 eV at room temperature. ZnO is non-toxic and non-expensive material which makes it very convenient for a large scale application. With the intensive development of nanotechnologies, ZnO found some new areas of application by using its nanosized form, namely ZnO nanoparticles (ZnONPs). Based on the fact that by changing the morphology, surface area, particle size and distribution, the properties of the same chemical compound can be varied, the antibacterial [1,2,3] and photocatalytic properties [4,5] of ZnONPs as well as their application for solar cells fabrication [6,7] have been extensively explored.

Promising results in each of the listed areas have been reported so far. Beek et al. [6] have described new hybrid bulk-heterojunction solar cells based on nanocrystalline ZnO with 5 nm diameter as the n-type semiconductor, which were prepared via hydrolysis and condensation of zinc acetate dihydrate. The ZnO nanoparticles were dispersed in a semiconducting polymer thus forming the active layer of the solar cell. This model cell demonstrated up to 40 % conversion of solar energy into electrical current proving the effectiveness of synergism of organic and inorganic materials in photovoltaics.

The photocatalytic activity of ZnONPs have been studied for years and the research is still ongoing due to the promising results. Weerathunga et al. [5] showed very interesting results from their latest study which suggests a relationship between the morphology of ZnO nanoparticles and their photocatalytic activity. Three types of shapes (rods, plates and cones) have been tested in the reaction of benzyl alcohol oxidation. The experimental data revealed that ZnO nanocones resulted in higher benzyl alcohol conversion compared to nanorods and nanoplates. This was explained by the crystal structure of ZnO nanocones and the orientation of undercoordinated O atoms towards the species in reaction medium. The authors are hopeful that their findings will provide useful insights how to optimize reaction conditions in other heterogeneous photocatalytic reactions involving oxidation reactions activity.

The antibacterial activity of ZnO is another area of interest of researchers. Bhuyan et al. [**Грешка! Показалецът не е дефиниран.**] used 25% (w/v) of *Azadirachta indica (Neem)* leaf extract for biosynthesis of ZnO nanoparticles. They tested the antibacterial and photocatalytic activity of ZnO obtained. By shake flask method different concentrations of ZnO nanoparticles (20 mg/mL, 40 mg/mL, 60 mg/mL, 80 mg/mL and 100 mg/mL) were used against Gram-positive and Gram-negative bacteria: *Staphylococcus aureus, Streptococcus pyogenes* and *Escherichia coli*. The authors found that increase in nanoparticle concentration leads to decrease in bacteria growth and Gram-positive bacteria were more sensitive to ZnO nanoparticles than Gram-negative bacteria. As an additional benefit, biosynthesized ZnO nanoparticles demonstrated activity in the photocatalytic degradation of methylene blue (MB) under the UV light.

Other authors also reported biosynthesis using plant extract for nanosized ZnO preparation. [8, 9, 10]. Salam et al. [10] have showed the synthesis of ZnONPs using *Ocimum basilicum L. var. purpurascens Benth.-Lamiaceae* leaf extract and zinc nitrate. The obtained ZnONPs had hexagonal (wurtzite) shape and size about 50 nm.

Other widely applied method for preparation of ZnONPs is by precipitation reaction under ultrasonic irradiation that allows a control over the size and morphology of the formed nanoparticles. This fact is of significant importance because some studies suggest that photocatalytic properties of ZnO strongly depend on their morphology [**Грешка! Показалецът не е дефиниран.**,11,12]. The effect of ultrasonic irradiation was confirmed by other research teams as well [13]. Meronia et al investigated an ultrasound-assisted synthesis of ZnO-based photocatalysts for the removal of NOx. They found enhanced surface area under sonication in comparison with samples from conventional synthesis. . The main experimental parameter affecting the structure of obtained ZnONPs was pH and the reaction temperature, as both influenced the precipitation of $Zn(OH)_2$ and its subsequent conversion to ZnO phase. Other important founding was that the counter-ion in the zinc precursor influence the morphology (star-shaped, flower-like, platelets), as well as the surface area [13].

In order to improve the antibacterial and photocatalytic properties of ZnONPs some authors suggest to immobilize the ZnO onto a support aiming a synergetic effect of action and easier recovery of the nanocomposite material. Zeolite is very beneficial support for ZnONPs because zeolite itself is used in water treatment as a sorbent and ion exchanger [14,15]. Shaw et al., demonstrated the efficiency and specificity of ZnO-zeolite core-shell composite in the removal of heavy metal ions and organic pollutants in neat, multi and mixed system [14]. It was established that the adsorption by the nanocomposite follows the order Pb(II) > Fe(III) > Cd(II) and MB dye > p-nitrophenol > Aniline. In addition, it was also demonstrated that the adsorption on zeolites is slower chemisorption compared to the faster physi-chemisorption in core-shell particles contributing to the rapid and enhanced adsorption posessed by the composite. ZnO-zeolite has also proven to be very effective photocatalyst and a multifunctional adsorbent with high specificity towards Pb(II), Fe(II), MB dye and p-nitrophenol.

For preparation of nanocomposite materials containing ZnONPs the ultrasonication method was chosen by researchers [16]. Heidaria et al. [17] used sonoprecipitation for in-situ preparation of Zn-zeolite nanocomposites resulting in novel ZnO nanorods over ion

exchanged clinoptilolite. This material was found to be efficient catalyst for the photocatalytic degradation of the drug furosemide (FRS). The higher surface area of the composite resulted in an enhanced photocatalytic activity in comparison to pristine ZnONPs prepared by conventional precipitation method. By means of various analytical methods (TEM, EDX, BET, UV-visible spectroscopy techniques, XRD, etc.) it was shown that the average particle size of ZnO in ZnO/clinoptilolite composite prepared by sonoprecipitation was 20.5 nm, while without sonication the size increased up to 34.8 nm. Aside from that, the sonication of the reaction mixture during the precipitation process prevented the agglomeration of nanoparticles. The effects of different parameters such as amount of ZnO on the zeolite, catalyst dosage, initial FRS concentration, pH of reaction media on the photocatalytic degradation were investigated.

ZnO-based composites are also known for their antibacterial properties against bacterial growth in wastewater.

Having in mind the above-described we have decided to use natural zeolite clinoptilolite for immobilization of ZnO and to study the potential of composites obtained for reduction of organic pollutants and inhibition of bacterial growth in wastewaters. In order to synthesize nanosized ZnO with well-developed surface area and uniform size distribution in pristine form and supported on zeolite, we applied the method of precipitation assisted by sonication. The present paper describes the preparation of ZnO nanoparticles and composite ZnO-zeolite and the characterization of as prepared materials by XRD, SEM and UV-Vis spectroscopy. The physicochemical parameters of these materials were examined and compared in respect to their morphology, composition and nanoparticles distribution.

2. Materials and methods

Zinc acetate dihydrate ($Zn(CH_3COO)_2 \cdot 2H_2O$) was purchased by Merck KGaA, sodium hydroxide (NaOH) from Valerus, Bulgaria. All reagents were used without any further purification. A natural zeolite (clinoptilolite) from the region of East Rhodopes, Bulgaria, was washed and modified by turning it to its sodium form, by placing the clinoptilolite in contact with 2 M NaCl as described in our previous paper [18]. The ultrasonic bath (SIEL UST7.8-200, with an ultrasound energy of 250 W) was used to generate the ultrasonic waves in the reaction mixture. The crystalline structure of the samples was determined by X-ray diffraction (XRD) Empyrean (PANalytical). UV–vis Diffuse Reflectance Spectroscopy (DRS) analysis was carried out on an Evolution 300 UV-Vis Spectrophotometer (Thermo Fisher Scientific), at room temperature in the wavelength range of 200–1100 nm). Scanning electron microscopy (SEM) was performed on JEOL 6390 и INCA Oxford element analyzer.

2.1 Synthesis of pristine ZnO nanoparticles by sonication

The experimental setup used is shown in Fig. 1. ZnO nanoparticles were synthesized by precipitation reaction between zinc acetate solution and sodium hydroxide solution under ultrasound irradiation. Overall amount of 12.5 cm^3 NaOH solution (0.1M) and 6.5 cm^3 $Zn(CH_3COO)_2$ solution (0.1M) were simultaneously added dropwise to a 50 cm^3 pure water and mixed under constant sonication for 30 min to form a precipitate. Prior to mixing of both solutions, the flask was immersed in the ultrasonic bath. . The resulting dispersion containing ZnONPs went further aging process for 1 h at 80^{o}C under sonication, after that the precipitate was filtered and washed with distilled water several times. The product was dried for 12 h at 120 ^{o}C and the resulting ZnONPs were further analyzed.

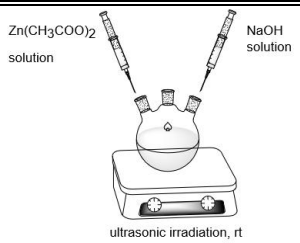


Fig. 1 *Schematic representation of experimental setup for ultrasonic synthesis of ZnONPs and ZnO-zeolite nanocomposites.*

2.2 Synthesis of ZnO-zeolite nanocomposite by sonication

ZnO-zeolite nanocomposite was prepared following the above described procedure and experimental setup shown inFig.1. Sodium form of clinoptilolite with a mass 0,5 g was dispersed in 60 cm^3 distilled water and sonicated for 15 min for surface groups activation. After that following the previously described procedure, 62.0 cm^3 NaOH solution (0.1M) and 31.0 cm^3 $Zn(CH_3COO)_2$ solution (0.1M) were added dropwise to the zeolite dispersion under constant ultrasonic irradiation for 30 min. The resulting reaction mixture was left to age for 1 h at 80 ^{o}C under sonication, after that the precipitate was filtered and washed with distilled water several times. The nanocomposite product was dried for 12 h at 120 ^{o}C and the resulting ZnO-zeolite was further analyzed.

3. Results and discussion

3.1 Materials characterization

We have successfully prepared ZnONPs and ZnO-zeolite nanocomposite by controlled precipitation reaction between $Zn(CH_3COO)_2$ and NaOH solutions under ultrasonic irradiation of the reaction mixture. The XRD crystalline analysis (Fig. 2) of the composite material confirmed the formation of ZnO nanoparticles with hexagonal wurtzite structure. The XRD patterns revealed that clinoptilolite was the major crystalline phase (82 wt.% clinoptilolite) and some cristobalite (2 wt.%) also existed as a naturally occurring inclusion. The ZnO phase was detected by its low intensity peaks showing that ZnONPs are part of the composite material. The percent of ZnO determined was 16 wt.%. The XRD data indicated that clinoptilolite is monoclinic phase, cristobalite is tetragonal and ZnO nanoparticles have hexagonal wurtzite structure.

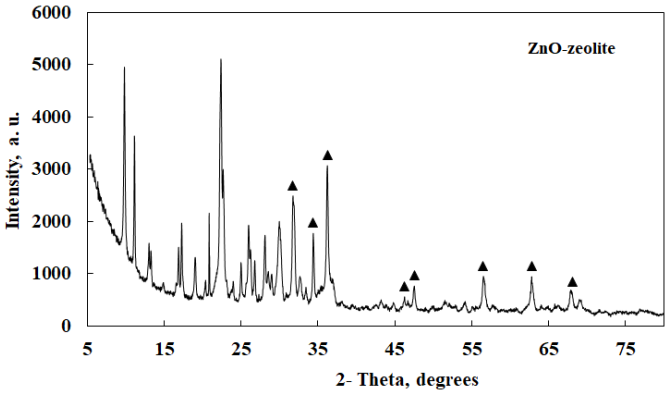
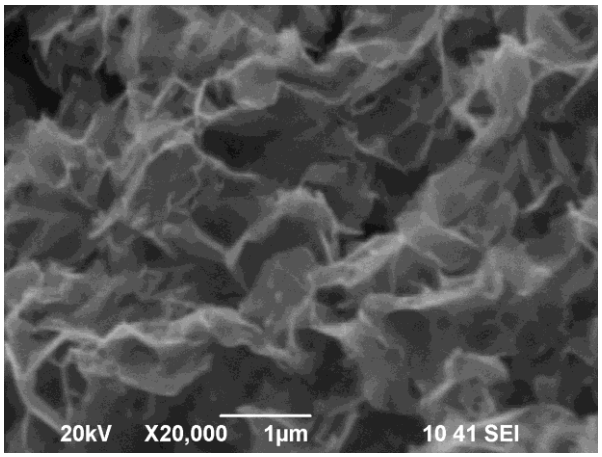


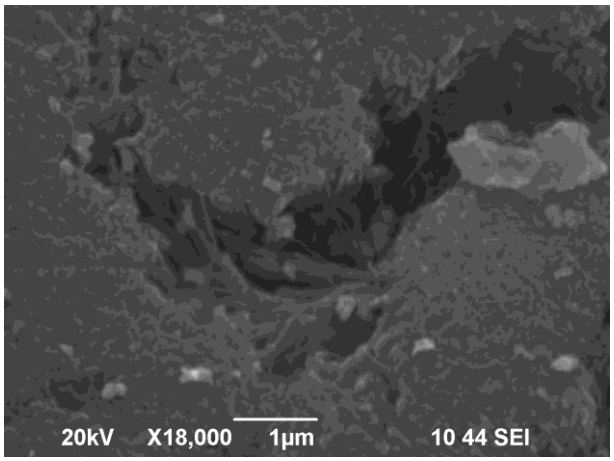
Fig. 2*. X-ray diffraction patterns of ZnO-zeolite nanocomposite. The peaks of ZnO phase are denoted with a black triangle. Detailed XRD analysis revealed the following composition: 82% clinoptilolite , 16% ZnO - and 2% cristobalite -.*

The surface morphology of ZnONPs and ZnO-zeolite nanocomposite was studied by SEM. Selected images of both materials are shown in Figure 3. SEM analysis revealed that the

ZnO has a flake like morphology (Fig. 3a). The nanocomposite ZnO-zeolite demonstrated that ZnO is evenly distributed onto the zeolite surface and the average size of the particles is about 100 nm (Fig. 3b).



(A)



(B)

***Fig. 3**. SEM images of sample of ZnONPs (A) and ZnO-zeolite nanocomposite (B).*

The SEM images strongly suggest that the presence of zeolite affects the formation and morphology of ZnO nanoparticles loaded on zeolite. In the case of ZnONPs, a flake-like nanomaterial (Fig. 3a) was obtained and in the case of ZnO-zeolite, when the zeolite was present in the reaction mixture spherical shaped nanoparticles were formed.

The results from EDX elemental analysis were summarized in Table 1. The estimated element composition in ZnO-zeolite nanocomposite revealed a ratio Al:Si equal to 1:5 that is typical for the studied natural clinoptilolite. The high percent of Zn (30.73) suggest that not only ZnO present but also Zn^{2+} ions might be exchanged with the zeolite prior precipitation and remained in the zeolite. .

***Table 1:** Element composition (in wt. %) of ZnO-zeolite nanocomposite as determined by EDX probe.*

Elements	O	Al	Si	K	Zn
ZnO-zeolite	39,71	4,66	23,63	1,26	30,73

Another evidence for Zn^{2+} ion exchange is the fact that no Na^+ ions were detected by EDX. It is because the Na^+ ions had been replaced by Zn^{2+} ions. It is also possible the Zn^{2+} ions adsorbed on the zeolite to react with OH^- ions from solution to form $Zn(OH)_2$ which further converts to ZnO nanoparticles that indicates the active role of zeolite support in the formation of ZnONPs on the zeolite surface.

UV–vis Diffuse Reflectance Spectroscopy analysis was carried out to characterize the optical properties of ZnO-zeolite composite. The spectrum is shown in Fig. 4. The weak band at 257 nm is due to zeolite framework and it originated from the charge transfer from O^{2-} to Al^{3+} ions at specific locations such as surface defects, corners, etc [19]. The intensive band at 360 nm is assigned to ZnO nanoparticles and confirms the nanosized ZnO on the clinoptilolite [20].

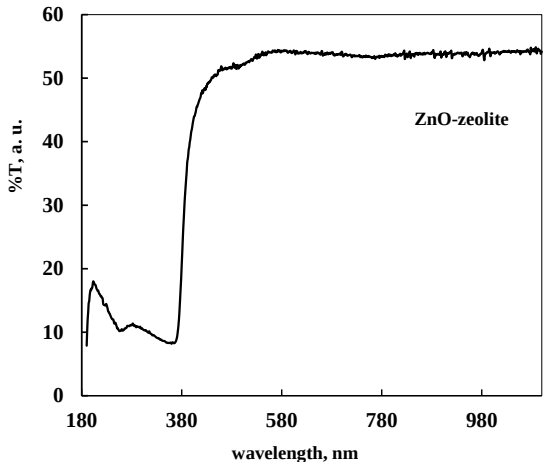


***Fig. 4**. UV–vis Diffuse Reflectance Spectrum of ZnO-zeolite nanocomposite.*

4. Conclusions

We have successfully prepared ZnO nanoparticles and ZnO-zeolite nanocomposite via precipitation reaction of $Zn(CH_3COO)_2$ and NaOH solution under ultrasonic irradiation. The XRD analysis confirmed that ZnO nanoparticles in the nanocomposite have hexagonal wurtzite structure.

The SEM images revealed different morphology of the prepared ZnONPs and ZnO-zeolite. The ZnONPs have flake-like shape while ZnO nanoparticles in the nanocomposite are spherical with average size of 100 nm. This observation suggests that zeolite plays an active role in the process of formation and nucleation of ZnONPs. The EDX element analysis showed an absence of Na^+ ions suggesting that they had been replaced by Zn^{2+} ions. It suggested electrostatic interaction or partial coordination bonding between the active sites in zeolite and ZnO nanoparticles in the composite.

In conclusion, the obtained ZnO-zeolite nanocomposite may be considered as a promising candidate material for water treatment. Such materials will be further tested for their photocatalytical and antibacterial activity.

4. Acknowledgements

The authors express gratitude to The Bulgarian National Science Fund (BNSF) for the financial support under Project DN-17/20.

5. References

1. A. C. Janaki, E. Sailatha, S. Gunasekaran, Spectrochim Acta A, 144, 17 (2015)

2. M. Sundrarajan, S. Ambika, K. Bharathi, Adv Powder Technol ., 26(5), 1294 (2015)

3. T. Bhuyan, K. Mishra, M. Khanuja, R. Prasad, A. Varma, Mater Sci Semicond Process, 32, 55 (2015)

4. S. Dey, S. Das, A. K. Kar, Mater. Chem. Phys., 270, 124872 (2021)

5. H. Weerathunga, C. Tang, A. J. Brock, S. Sarina, T. Wang, Q. Liud, H. Zhu, A. Du, E.R. Waclawik, J. Colloid Interface Sci., 606(1), 588 (2022)

6. W. J. E. Beek, M. M. Wienk, R. A. J. Janssen, Adv.Mater, 16(12), 1009 (2004)

7. M. Saeidi, M. Abrari, M. Ahmadi, *Appl. Phys. A* **125,** 409 (2019).

8. F.T. Thema, E. Manikandan, M.S. Dhlamini, M. Maaza, Mater. Lett., Volume 161, 24 (2015)

9. G. Yashni, A. Al-Gheethi, R. M. S. R. Mohamed, N. Vo Dai-Viet, A. A.Al-Kahtani, M. Al-Sahari, N. J. N. Hazhar, E. Nomand, S. Alkhadher, Chemosphere, 281, 130661 (2021)

10. H. A. Salam, R. Sivaraj, R. Venckatesh, Mater. Lett, 131, 16 (2014)

11. S.R. Veerabhadraiah, S. Maji, A. Panneerselvam, J. Cryst. Growth, 14, 126430 (2021)

12. Z. Sharifalhoseini, M. H. Entezari, R. Jalal, Ultrason Sonochem 27, 466 (2015)

13. D. Meronia, C. Gasparini, A. Di Michele, S. Ardizzone, C. L. Bianchi, Ultrason Sonochem 66, 105119 (2020)

14. R. Shaw, T. Mittal, S. Tiwari, S. K. Tiwari, J. Environ. Chem. Eng. 6, 1424 (2018)

15. V. R. Batistela, L. Z. Fogaca, S. L. Fávaro,W. Caetano, N. R. Camargo Fernandes-Machado, N. Hioka, Colloids Surf. A: Physicochem. Eng. Asp. 513, 20 (2017)

16. X. Li, H. Li, X. Wang, D. Xu, T.g You, Y. Wu, F. Xu, Int. J. Biol. Macromol. 183, 760 (2021)

17. Z. Heidaria, R. Alizadeha, A. Ebadia, N. Oturan, M.A. Oturan, M. Sep. Purif. Technol., 242, 116800 (2020)

18. M. Panayotova, N. Mintcheva, G. Gicheva, L. Djerahov, N. Mirdzveli, Proceedings of 20th International Multidisciplinary Scientific GeoConference SGEM 2020, Albena, Bulgaria, 18 - 24 August 2020; p. 77-84

19 I. Rodríguez Iznaga, V. Petranovskii, G. Rodríguez Fuentes, C. Mendoza, A. Benítez Aguilar, J. Colloid Interface Sci. 316, 877 (2007).

20 T.B. Ivetic, M.R. Dimitrievska, I.O. Guth, Lj.R. Dacanin, S.R. Lukic-Petrovic, J. Phys. Res. 36 (1), 43 (2012)

Electron Beam Melting and Refining of Copper

Asya Asenova-Robinzonova[1], Lilyana Koleva[1,*], Elena Koleva[1,2,**], Vania Vassileva[2], Katia Vutova[2]
University of Chemical Technology and Metallurgy, Bulgaria[1]
Institute of Electronics, Bulgarian Academy of Sciences, Bulgaria[2]
*sura@uctm.edu, **eligeorg@uctm.edu

Abstract: *Experimental results for the quality of electron beam melting and refining of pyro-refined copper samples are analysed by an empirical model estimation approach. Investigation of the influence of the process parameters – melting power and time of refining on the removal efficiency of specific impurities, overall removal efficiency and material losses is performed.*
Keywords*: ELECTRON BEAM REFINING, COPPER, REMOVAL EFFICIENCY, MATERIAL LOSSES, ELECTRON BEAM MELTING*

1. Introduction

Copper (Cu) is one of the most important metals used in modern life and up to 50% of Cu production is used for making cables, heat exchangers, vacuum equipment, etc., and about 40% is used for production of different alloys with: Zn, Sn, Al, Ni and other valuable metals, which are needed for a number of industries.

The electron beam melting and refining (EBMR) of metals and alloys in vacuum is done using electron beam as a heating source. The aim of the metallurgical refining processes is the removal of metallic impurities and reduction of non-metallic components from the raw material. The increasing demand for purity of the produced materials has led to the use of water-cooled copper crucible in furnaces during EBMR, where the initial material is melted, refined and re-solidified without pollution at using a ceramic pot, and thus EBMR method is superior to the refining methods of the conventional metallurgy [1, 2].

In this paper, investigation of the influence of the process parameters – melting power and refining time on the refined quality characteristics – the removal efficiency of specific impurities, overall removal efficiency and the material losses, is performed based on empirical model estimation.

2. Response surface methodology

Response surface methodology is a group of mathematical and statistical procedures used in fitting an empirical model to the experimental data obtained in relation to an experimental design [3]. Regression models or the polynomial models of some order, giving an adequate functional relationship between a response of interest y (performance characteristic) and a number of associated control (or input) variables (process parameters) $x_1, x_2, \dots x_m$, are estimated:

$$\hat{y}(\vec{x}) = \sum_{i=1}^{k} \hat{\theta}_i f_i(\vec{x}), \quad (1)$$

where $\hat{\theta}_i$ are the estimates of the coefficients in the regression model.

The natural values of the factors (z_i) in the regression models are coded in the region [-1 ÷ 1] and the relation between the coded (x_i) and the natural values (z_i) is given by:

$$x_i = (2z_i - z_{i,max} - z_{i,min})/(z_{i,max} - z_{i,min}), \quad (2)$$

where $z_{i,min}$ and $z_{i,max}$ are the corresponding values of the minimum and the maximum of the process parameters during the experiment.

3. Experimental conditions

Electron beam melting and refining (EBMR) of Cu was performed using 60 kW equipment with one electron gun and a water-cooled copper crucible with diameter of 60 mm. The vacuum pressure in the melting chamber was in the range 5-8×10^{-3} Pa.

Two EBMR process parameters are varied in order to investigate the EBMR process of copper - z_1 is the electron beam power and z_2 – the refining time. The values of the electron beam powers were: 7.5 kW, 10 kW and 15 kW, while the refining times were set to different values in the range between 3 and 30 minutes [4, 5]. Fifteen experiments were performed for different combinations of these process parameters. The measured quality characteristics are the following: the removal efficiency of Sn (y_1, %), removal efficiency of Ag (y_2, %), removal efficiency of Zn (y_3, %), overall removal efficiency (y_4, %) and the material losses (y_5, g).

4. Estimation of regression models

The dependencies of the quality characteristics of the refined Cu: y_1 – the removal efficiency of Sn [%], y_2 – the removal efficiency of Ag [%], y_3 – the removal efficiency of Zn [%], y_4 – the overall removal efficiency [%] and y_5 – the material losses [g] on the variation of the process parameters: z_1 – the melting power [kW] and z_2 – the refining time [min] are estimated.

They are presented for coded in the region [-1 ÷ 1] values of the process parameters in Table 1, together with the square of the multiple correlation coefficient R^2 and the square of the adjusted multiple correlation coefficient R^2_{adj}. The values of both coefficients are high (maximum 100 %) and the estimated models can be considered as good enough for prediction and investigation.

Table 1: *Regression models.*

	Regression models	R^2 *[%]*	R^2_{adj} *[%]*
$\hat{y}_1(\vec{x})$	$99.388388 + 0.96370857x_1 + 0.08831581x_2 - 0.3525x_1^2 - 0.09437149x_1x_2$	99.89	99.84
$\hat{y}_2(\vec{x})$	$97.442395 + 0.05581727x_1 - 0.03479241x_2 - 0.15916955x_1x_2$	95.01	93.64
$\hat{y}_3(\vec{x})$	$94.047439 - 7.8928562x_2 - 7.120348x_1x_2 - 6.641097x_1x_2^2$	73.97	66.87
$\hat{y}_4(\vec{x})$	$98.759141 - 4.3757779x_2^2 - 3.1445406x_1x_2 + 4.3840616x_1^2x_2 + 4.2965256x_1x_2^2$	80.73	73.02
$\hat{y}_5(\vec{x})$	$9.638259 + 8.4167181x_1 + 7.4642417x_2 + 6.5539856x_1x_2$	99.99	99.99

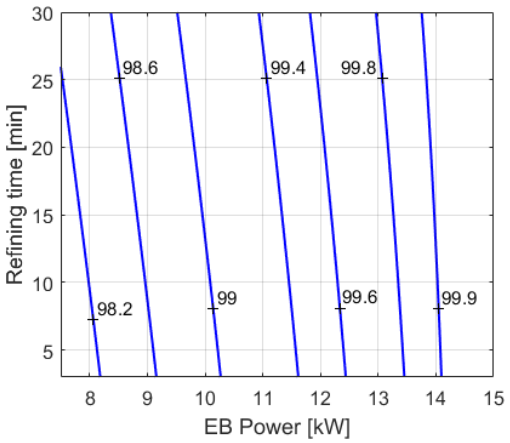


Fig. 1 *Contour plot of the removal efficiency of Sn – y_1, depending on the variation of the melting power (z_1) and the refining time (z_2).*

The obtained by QstatLab [6] regression models for the investigated quality characteristics are used for the investigation of the process of electron beam refining of Cu.

In Fig. 1 – Fig. 3 contour plots of the removal efficiency of Sn – y_1, removal efficiency of Ag – y_2 and removal efficiency of Zn – y_3 depending on the variation of melting power (z_1) and the refining time (z_2) are presented.

From Fig. 1 it can be seen that the removal efficiency of Sn is 99.9%, if the EB power is higher than 14 kW regardless of the chosen refining time in the investigated range.

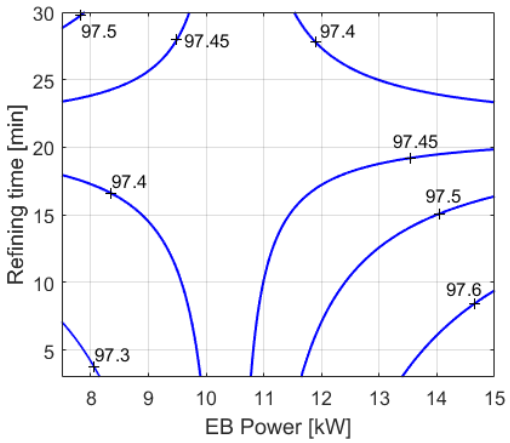


Fig. 2 *Contour plot of the removal efficiency of Ag – y_2, depending on the variation of the melting power (z_1) and the refining time (z_2).*

Fig. 2 shows the contour plot of the removal efficiency of Ag. It can be seen that the removal efficiency is 97.4% or more, but the maximum value (97.6%) is obtained in the range of working regimes where the refining time is less than 6 [min] and the EB power is higher than 14 kW.

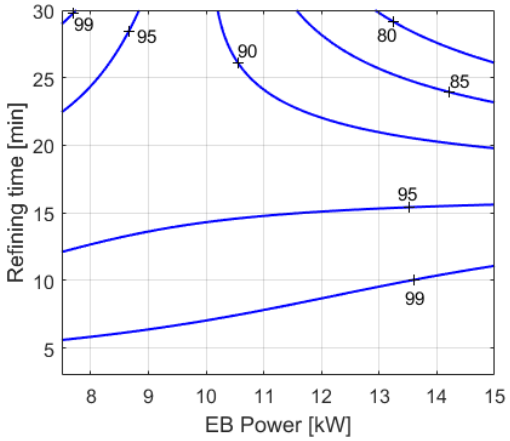


Fig. 3 *Contour plot of the removal efficiency of Zn – y_3, depending on the variation of the melting power (z_1) and the refining time (z_2).*

From Fig. 3 it can be seen that the removal efficiency of Zn can be 99%, if the refining time is equal to 5 min regardless of the chosen EB power or for EB powers higher than 13 kW and refining time less than 8 min.

The contour plot shown in Fig. 4 represents the overall removal efficiency (y_4) depending on the variation of melting power (z_1) and the refining time (z_2). It can be seen that the highest overall removal efficiency can be obtained, if the refining time is in the region from 17 min to 23 min and the EB power is set on its minimal value (less than 8 kW) or the EB power is higher than 14.7 kW and the refining time is more than 20 min.

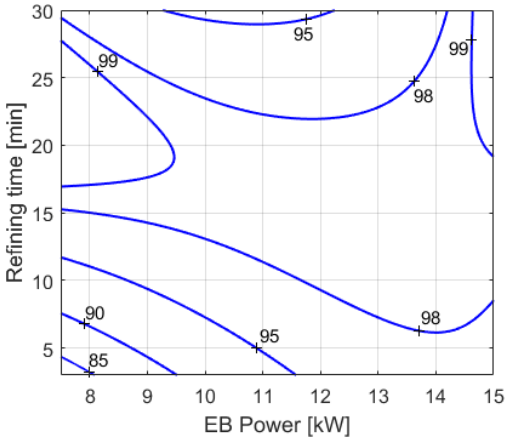


Fig. 4 *Contour plot of the overall removal efficiency – y_4, depending on the variation of the melting power (z_1) and the refining time (z_2).*

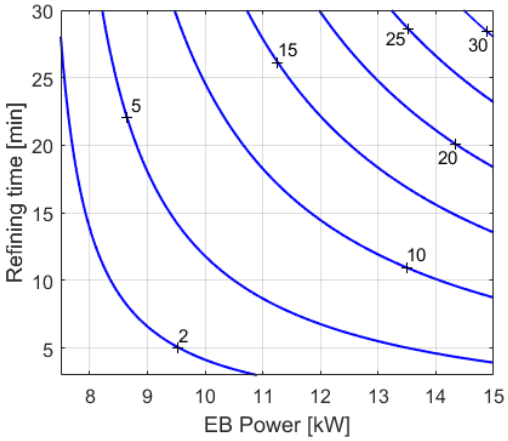


Fig. 5 *Contour plot of the material losses – y_5, depending on the variation of the melting power (z_1) and the refining time (z_2).*

Fig. 5 represents the investigation of the material losses during the process electron beam melting and refining of pyro-refined copper. From the contour plot it can be seen that the losses under 2 g can be obtained, if the EB power is less than 8.5 [kW] and the refining time is less than 7 min.

5. Correlation analysis

Another way to analyze the removal efficiencies of different inclusions is to analyze the coincidence of the refining process parameters in direction of simultaneously removing the inclusions or if a certain set of process parameters favors the refining of one of the inclusions at account of another inclusion. Correlation analysis can answer the question for presence of such correlation between different pairs of inclusions.

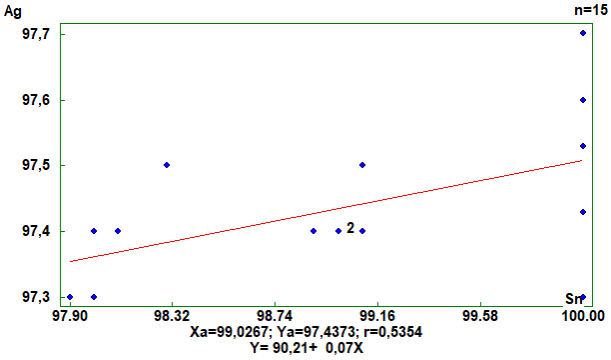


Fig. 6 *Scatter plot of the removal efficiency of Sn – y_1 and Ag – y_2.*

In Fig. 6 – Fig. 8 the scatter plots for the different combinations of inclusion removal efficiencies obtained by QstatLab [6] are presented.

From Fig. 6 it can be seen that there is moderate positive linear relationship between the removal efficiencies of Sn and Ag. The correlation coefficient is r_1 = 0.54 and performed test for significance defines it as a significant correlation. This means, that the choice of EBMR process parameters that favor the refining of Sn will favor the refining of Ag as well.

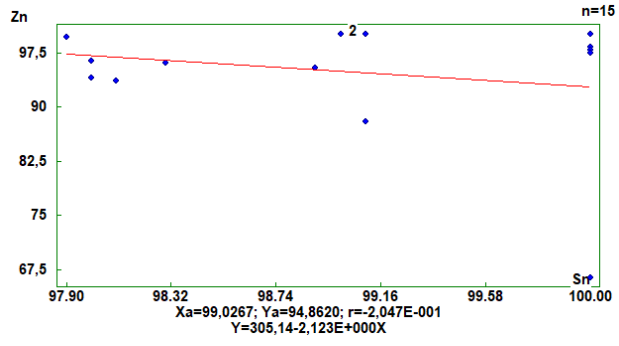


Fig. 7 *Scatter plot of the removal efficiency of Sn – y_1 and Zn – y_3.*

Fig. 7 shows that there is no significant correlation between the removal efficiencies of Sn and Zn. The Pearson linear correlation coefficient is small and insignificant.

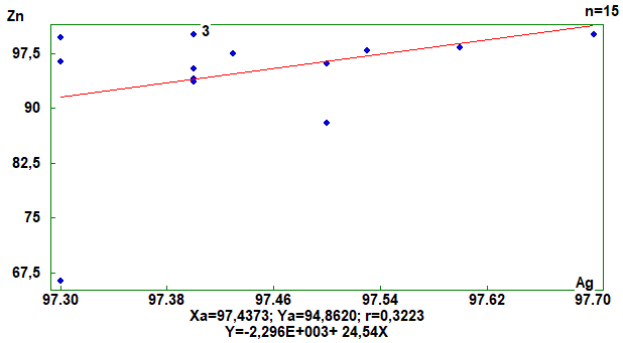


Fig. 8 *Scatter plot of the removal efficiency of Ag – y_2 and Zn – y_3.*

Fig. 8 shows week positive correlation between the removal efficiencies of Ag and Zn – the Pearson linear correlation coefficient is 0.32. After making hypothesis testing for its significance it is proven as insignificant correlation coefficient.

Consequently, the only significant correlation found is between the removal efficiencies of Sn and Ag. The choice of optimal EBMR refining process parameters should be made according the technological requirements for all quality characteristics and compromise solutions should be found that favors the refining of one or another of the inclusions to a certain extend.

5. Conclusions

Regression models for the removal efficiency of specific impurities, overall removal efficiency and the material losses depending on the variations of the electron beam melting and refining process parameters at Cu melting were estimated.

The obtained regression models can be used for future investigation and optimization of the process electron beam melting and refining of pyro-refined copper.

Acknowledgements

The authors want to thank for the financial support of the projects KP-06-N27/18 and DN17/9, funded by the National Fund "Scientific Investigations".

References

1. G. Mladenov, E. Koleva, K. Vutova, V. Vasileva, *Experimental and theoretical studies of electron beam melting and refining, Chapter in a special review book: Practical Aspects and Applications of Electron Beam Irradiation*, (eds.: M. Nemtanu, M. Brasoveanu, publ. Research Signpost/Transworld Research Network) 43-93 (2011).
2. K. Vutova, K. Koleva, G. Mladenov, IREME – spec. Iss. on Heat Transfer, **5**, 257-265 (2011)
3. M. A. Bezerra, R. E. Santelli, E. P. Oliveira, L. S. Villar, L. A. Escaleira, Talanta, **76**, 965-977 (2008)
4. V. Vassileva, K. Vutova, M. Markov. J. of Phys. Conf. Ser. 2021. Proc. Int conf. VEIT'21 (accepted)
5. I. N. Vuchkov, L. N. Boyadjieva, *Quality improvement with design of experiments* (Kluwer Academic Publishers: The Netherlands, 2001)
6. QstatLab home page: http://www.qstatlab.co.uk/eng/index.html

Fabrication of the Porous Structures with Gradient Thickness of the Struts, by using FDM 3D Printing with Dynamically Changed Parameters during the Printing

Nikola Palic[1,*], Fatima Zivic[1], Vukasin Slavkovic[1], Nenad Grujovic[1]
Faculty of Engineering, University of Kragujevac[1]
palic@fink.rs

Abstract: *This paper deals with 3D printing of porous, functionally graded structures by using Fused Deposition Modeling (FDM). We investigated the printing parameters that can allow printing with gradual infill and challenges associated with this method of printing. We fabricated polylactic acid (PLA) porous structures with variable infill by using FDM 3D printing. Set of the printing parameters for variable infill were investigated: gradient infill and gradient speed and the most successful case is shown. The significant influence of the printer hardware elements was noticed, among which, the worn gear tooth and inadequate extruder feed model can result in inability to print functionally graded lines.*
Keywords*: FUNCTIONALLY GRADED POROUS STRUCTURES; FDM 3D PRINTING; GRADIENT INFILL, DYNAMIC EXTRUSION, PRINTING ERRORS*

1. Introduction

The ability to produce structures/parts with locally variable structure and composition, such as porous, cellular, and lattice structures, is important for scientific and technological advancement in a variety of fields, ranging from tissue engineering [1, 2], bone grafts and dental implants [3, 4] to aerospace engineering [5] and microelectronics [6]. Several approaches have been presented to create these heterogeneous structures [7, 8, 9, 10]. Functionally Graded Materials (FGM) can efficiently mimic the natural structures, such as the bone structure [3, 4], thus providing artificially designed and produced implants closely resembling the natural organs and tissues. Functionally graded additive manufacturing can be realised in different ways [11], whereas additive manufacturing (AM) or 3D printing, offers the most promising possibilities in the FGM design [8, 12, 13]. One of the main benefits of the FGMs is the possibility to tailor mechanical properties of the constructs [14]. However, AM technologies are still associated with certain challenges in producing FGMs [15, 16].

Functionally Graded Materials (FGMs) are heterogeneous materials with tailored composition and structural gradients that have specified qualities in the desired orientation [17, 18, 19]. Functionally Graded Cellular Structures (FGCS) are Cellular Structures that have been functionally graded and are being investigated for a variety of engineering applications [20]. When opposed to totally porous materials, functionally graded porous structures have the benefit of preserving strength close to solid structures [21].

Functional graded materials expands the design space by allowing the engineer to tailor distinct material qualities throughout the different zones within the same element [14]. Objects with FGM structure, in essence, allow engineers to customize its design beyond simply modifying its physical shape to fit design aims and restrictions. FGM structures are challenging to design because it should allow modifications throughout the whole structure volume and is not limited only to topological or the dimensional variations. Such profound structural changes accompanied by the dynamic variation of the structural properties throughout the volume may pose significant complexities, and optimisation techniques are often used, from aspects of the final properties, topological optimization, material distributions, or the fabrication technologies [14, 22]. Furthermore, manufacturing limitations will most likely limit the available design zone and should be taken into account while planning [22].

For components or products with complicated and custom designs, 3D printing is one of the best suited technology, including the low cost Fused Deposition Modeling (FDM) 3D printing [23]. 3D printing of FGMs with broadly and diversely adjustable features in a single 3D printing process has steadily grown in relevance and has been intensively investigated recently, owing to benefits in structural control, resolution, and scalability, among others [16, 24].

Fused Deposition Modeling (FDM) or Fused Filament Fabrication (FFF) is a popular additive manufacturing (AM) technology that may be found in both open-source/low-cost and high-end/industrial AM systems. The typical AM manufacturing method is commonly followed for fabricating heterogeneous components with FDM/FFF [25]. The procedure starts with the creation of 3D models that use CAD software to directly create the desired geometrical form and structure. The geometrical information from these models is then sent to the relevant slicing and route planning software, which creates machine instructions files for the FDM/FFF system. The FDM/FFF technology is then used to create the parts, which are subsequently postprocessed and finalized according to the application [13].

It might be complex to select the printing parameters that will allow the desired porosity and pore size values in the case of a porous structure [20, 26]. The most process variables are related to the machine operation rather than the final form of the final component [20]. Furthermore, final porosity and pore size may deviate from theoretically designed values. Pore size and porosity of structures with gradient infill patterns are measured as a function of the several printing parameters . The influence of the printing parameters is significant, among which the infill values have the prominent role [27]. Application of 3D printing in design and fabrication of porous functionally graded structures are still in research [13, 26], including the investigation on correlation to the resulting material properties [28, 29].

This paper presents the fabrication of porous structures with variable infill by using FDM 3D printing, made of polylactic acid (PLA). We present the parameters of 3D printing for variable printing speed and printing flow and the printed structure with variable infill. We also present the issues in fabrication of such variable structures, related to the 3D printing process.

2. Materials and Methods

The polylactic acid (PLA) sample was created using FDM printer Creality CR-10S5 with purple filament (1.75 mm diameter) as the standard material. A disc with a diameter of 50mm and a height of 3mm serves as the sample (Fig 1a).

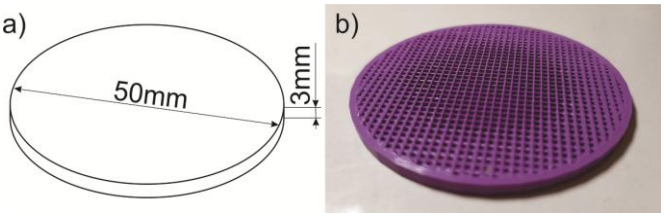


Fig. 1 *(a) schematic view of the printed sample, (b) printed sample*

All of the samples in this study were printed with a 0.4 mm nozzle. We used the printer default parameters, which included 30% infill, the layer height of 0.2 mm, and the printing speed of 20 mm/s. In total, the printing process lasted 29 minutes and 7 grams

of material was used. The printing parameters are given in Table 1. Layer height refers to the thickness of one layer during the 3D printing, while shell thickness refers to the thickness of the outer layers, as the printing head initially passes along the shell line and then fills it with layers. The thickness of the first and the final printing layers that were printed with full fill, regardless of the filling density settings, is referred to as bottom and top thickness. The filling of the specific printing elements is referred to as the infill density. The printing head speed during the printing along a straight line is referred to as the printing speed. The temperature of the nozzle during the printing is referred to as the printing temperature. To minimize the damage of the printed object, that can be caused by the sticking and non-homogenous stress distributions, the sample is printed on a heated plate (with defined bed temperature). Because it makes it easier to remove the final printed sample, raft is used as the support on which the object is directly printed.

Table 1: *3D printing parameters for the standard polylactic acid (PLA).*

Quality	
Layer height	0.2mm
Shell thickness	1.2mm
Enable retraction	Yes
Fill	
Bottom/Top thickness	0mm
Infill density	30%
Infill pattern	Line
Print speed and temperature	
Print speed	20mm/s
Printing temperature	230°C
Bed temperature	50°C
Support	
Support type	None
Platform adhesion type	Raft
Filament	
Diameter	1.75mm
Flow	100%

The sample was not printed with a standard constant infill but with a gradient infill. Gradient filling means that the filling grid volume is distributed unevenly over the sample. Different filler fiber thicknesses may be generated by adjusting the extra print settings inside the Ultimaker Cura software by using the gradient infill plugin. Fig. 2 shows the variation of the fiber thickness along the printing path.

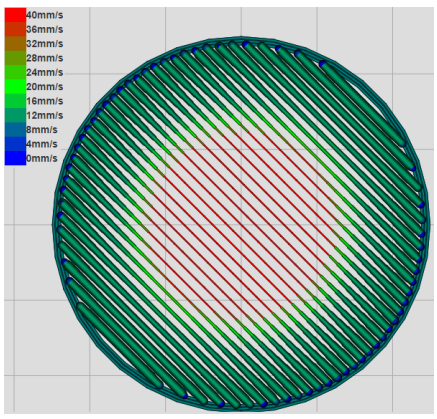


Fig. 2 *The distribution of the fiber thickness in the sample filling, depending on the variation of the printing speed.*

Printing parameters for obtaining variable infill are based on the variation of the printing speed and printing flow. With increasing the printing speed at constant flow, the fiber become thinner, while with increasing the printing flow at constant speed, the fiber become thicker. The distance gradient is a parameter that defines how far from the shell the speed and flow parameters will change. Gradient discretization represents the number of steps on how much the speed and fill parameters will change per gradient distance. 'Max flow' and 'Min flow' are the parameters that set up the limits of the range in which the flow varies during one gradient distance. 'Max over speed' and 'Min over speed' parameters determines the range of the printing speed that is used during one printing cycle. All of the gradient infill parameters are listed in Table 2.

Table 2: *Set of the printing parameters for variable infill*

Gradient infill	
Gradient distance	12mm
Gradient discretization	8
Max flow	350%
Min flow	50%
Short distance flow	350%
Gradient speed	
Max over speed	200mm/s
Min over speed	60mm/s

3. Results and discussion

The goal of the experiment is to leverage extrusion width variability to change the quantity of material that comes out of the nozzle during the printing in a real time. With the current designs and very slight flow alterations, the extruder may deposit more plastic near to the walls and decrease the flow in the middle. It is possible to perform it differently depending on the parameter settings: for example to strengthen the center zones and to make weaker outer zones towards the edges. We made samples that have weaker central zone and the porous structure becomes stronger towards the edges.

The samples were created in the shape of a disk to make it easier to see the effect of the parameters used to control the progressive infill on the sample. The zone of the intense filling of the material around the periphery of the sample is clearly visible in Figure 3a. This zone is 12 mm wide, which is the value of the gradient distance print parameter that has been specified (Table 2). The thickness of the printing lines at the ends and in the center of the sample are shown in Figure 3b. It can be seen that the lines in the central zone are half the thickness of the same printed line at the outer, edge zone. Considering the flow (max flow = 350 percent, min flow = 50 percent) and the speed (max speed 200mm/s, min speed 60mm/s) parameters, it is reasonable to deduce that such difference in fiber thickness might be considerably larger. However, major drawbacks of the lab 3D printers, especially FDM 3D printers, are related to the dimensional accuracy, and the high probability for some hardware elements (e.g. gear tooth) to rather rapidly loose their original performance, thus greatly influencing the final printed structures. For example, if the sliding of the filament occurs without direct feed into the extruder, the printing settings become inconsistent.

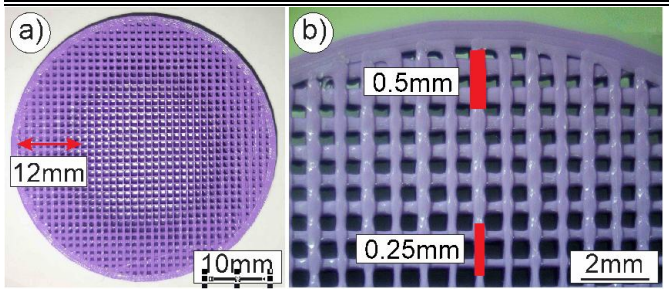


Fig. 3 *Gradient structure of the printed sample with two different magnifications*

Figure 4 shows the change in extrusion width along the diameter line printing direction. This variation of the extrusion width is directly correlated with the width of the printed line and produces its variation as shown in Fig. 3.

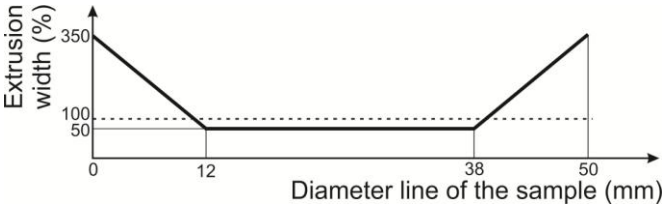


Fig. 4 *Change in extrusion width along the diameter line printing direction*

The success of the gradient infill printing is greatly influenced by the hardware settings and characteristics of the FDM printer. One of the characteristics of the printer that has the greatest influence is the performance of the extruder feed. There are two types of extruders, commonly used in FDM 3D printers: Bowden extruder and direct feed extruder (Fig. 5). Direct feed extruder gives better results because in Bowden extruder the filament is driven from a distance through the teflon tube. The distance that the filament has to travel has a negative influence on variable change of parameters during the printing, since the extruder can lose the ability to immediately apply the variations. Hence, in Bowden extruder, there is a slight delay in variation of parameters that significantly influence the possibility to print the gradient structure. Slightly delayed feed during the changing of the filament push speed produced the tube movement which further influenced delays in change of the fiber thickness, thus producing errors in printed structure: inaccurate change in the thickness of the fiber at the top of the nozzle.

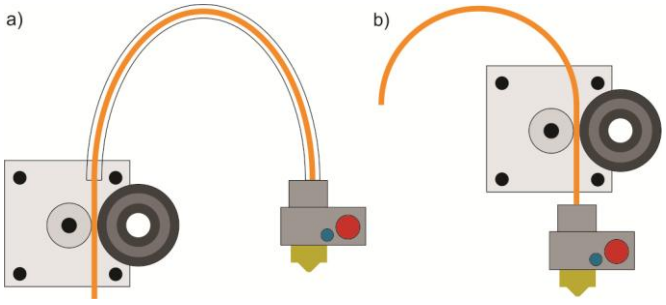


Fig. 5 *The extruder feed models: a) Bowden extruder, b) Direct feed extruder*

Filament slip during the feeding of the extruder is another possible source of error in the printed structure. Filament slip can occur for two main reasons. The first one is the insufficiently strong spring. For the proper filament feed, the spring creates tension and thus allows the gear to push the filament into the extruder. If the spring is weakened, what can occur after a certain time of the printer work, it will not create sufficient tension for the filament to be properly pushed. Another, much more common reason is the wear of the drive gear. In small 3D printers (home printers, fab lab printers), the drive gear is usually made of brass that does not exhibit high wear resistance, especially in harsh environments. Over time, the gear teeth wear out, thus forming worn tracks (channels), along which the filament slides (Fig. 6). This has a negative effect on the printing with standard parameters, and especially significant influence on the printing with a gradient infill. Worn gear teeth cannot efficiently follow the changes in the filament push speed and results in filament slipping, thus producing significant errors in the printed structure. This is especially prominent for the gradient infill printing where, in case of the worn teeth, we obtained structures with significantly different designs from the initially planned ones. Accordingly, we changed this gear element in the printer and used the new one, for the fabrication of the previously showed samples with gradient fill (Fig. 1b), since with the worn gear, it was impossible to produce them.

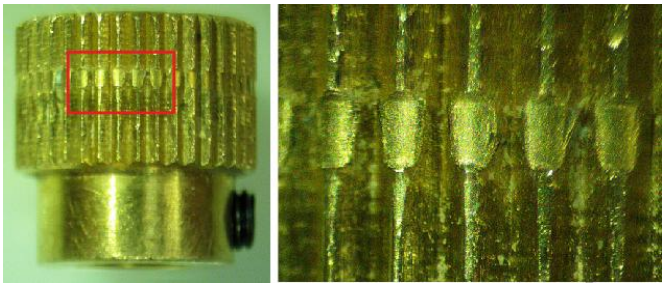


Fig. 6 *Worn brass gear that drives the filament*

4. Conclusion

Porous functionally graded PLA samples were fabricated using 3D printing (FDM) with the printing layer of 0.15 mm and gradient infill of 30%. Gradient infill printing was sucessfuly realised, proven by the functional distribution of the infill line thickness inside the sample structure. A variety of factors influenced the quality of the printed object. Beside the process parameters, the quality of the printer hardware elements essentially determines the behaviour during the printing. For the printing of porous, functionally graded structures, even the small defects in printer hardware can result in inability to print it. For the FDM 3D printing, the most significant influence, was determined to be the worn drive gear and extruder feed model. Further research on the influence of process parameters on the structural and mechanical properties will be realised.

5. Acknowledgement

This paper is funded through the EIT's HEI Initiative SMART-2M project, supported by EIT RawMaterials, funded by the European Union.

6. References

1. F. Hejazi, S. Bagheri- Khoulenjani, N. Olov, D. Zeini, A. Solouk, H. Mirzadeh, *Fabrication of nanocomposite/nanofibrous functionally graded biomimetic scaffolds for osteochondral tissue regeneration*, Journal of Biomedical Materials Research Part A, **109(9)**, 1657–1669, (2021).
2. S. V. Murphy, A. Atala, *3D bioprinting of tissues and organs*, Nature Biotechnology, **32(8)**, 773–785, (2014).
3. M. C. Bottino, V. Thomas, G. M. Janowski, *A novel spatially designed and functionally graded electrospun membrane for periodontal regeneration*, Acta Biomaterialia, **7(1)**, 216–224, (2011).
4. M. Mehrali, F. S. Shirazi, M. Mehrali, H. S. C. Metselaar, N. A. B. Kadri, N. A. A. Osman, *Dental implants from functionally graded materials: Dental Implants from FGM*, Journal of Biomedical Materials Research Part A, **101(10)**, 3046–3057, (2013).
5. J. W. Chua, X. Li, T. Li, B. W. Chua, X. Yu, W. Zhai, *Customisable sound absorption properties of functionally graded metallic foams*, Journal of Materials Science & Technology, **108**, 196–207, (2022).
6. Z. Rahimi, W. Sumelka, S. R. Ahmadi, D. Baleanu, *Study and control of thermoelastic damping of in-plane vibration of the*

functionally graded nano-plate, Journal of Vibration and Control, **25(23–24)**, 2850–2862, (2019).
7. J. M. Lowen, J. K. Leach, *Functionally graded biomaterials for use as model systems and replacement tissues*, Advanced Functional Materials, **30(44)**, 1909089, (2020).
8. N. Oxman, *Variable property rapid prototyping: Inspired by nature, where form is characterized by heterogeneous compositions, the paper presents a novel approach to layered manufacturing entitled variable property rapid prototyping*, Virtual and Physical Prototyping, **6(1)**, 3–31, (2011).
9. B. Kieback, A. Neubrand, H. Riedel, *Processing techniques for functionally graded materials*, Materials Science and Engineering: A, **362(1–2)**, 81–106, (2003).
10. D. Almasi, M. Sadeghi, W. J. Lau, F. Roozbahani, N. Iqbal, *Functionally graded polymeric materials: A brif review of current fabrication methods and introduction of a novel fabrication method*, Materials Science and Engineering: C, **64**, 102–107, (2016).
11. G. H. Loh, E. Pei, D. Harrison, M. D. Monzón, *An overview of functionally graded additive manufacturing*, Additive Manufacturing, **23**, 34–44, (2018).
12. U. Scheithauer, S. Weingarten, R. Johne, E. Schwarzer, J. Abel, H-J. Richter, T. Moritz, A. Michaelis, *Ceramic-based 4d components: Additive manufacturing (Am) of ceramic-based functionally graded materials (Fgm) by thermoplastic 3d printing(T3dp)*, Materials, **10(12)**, 1368, (2017).
13. J. Giannatsis, A. Vassilakos, V. Dedoussis, *A heterogeneous infill technique for fused deposition modeling*, Procedia Manufacturing, **51**, 642–648, (2020).
14. T. S. Lumpe, J. Mueller, K. Shea, *Tensile properties of multi-material interfaces in 3D printed parts*, Materials & Design, **162**, 1–9, (2019).
15. M. Bahraminasab, *Challenges on optimization of 3D-printed bone scaffolds*, BioMedical Engineering OnLine, **19(1)**, 69, (2020).
16. M. Ansari, E. Jabari, E. Toyserkani, *Opportunities and challenges in additive manufacturing of functionally graded metallic materials via powder-fed laser directed energy deposition: A review*, Journal of Materials Processing Technology, **294**, 117117, (2021).
17. M. Naebe, K. Shirvanimoghaddam, *Functionally graded materials: A review of fabrication and properties*, Applied Materials Today, **5**, 223–245, (2016).
18. M. Sathish, N. Radhika, B. Saleh, *A critical review on functionally graded coatings: Methods, properties, and challenges*, Composites Part B: Engineering, **225**, 109278, (2021).
19. R. Ghanavati, H. Naffakh-Moosavy, *Additive manufacturing of functionally graded metallic materials: A review of experimental and numerical studies*, Journal of Materials Research and Technology, **13**, 1628–1664, (2021).
20. Y. Li, Z. Feng, L. Hao, L. Huang, C. Xin, Y. Wang, E. Bilotti, K. Essa, H. Zhang, Z. Li, F. Yan, T. Peijs, *A review on functionally graded materials and structures via additive manufacturing: From multi- scale design to versatile functional properties*, Advanced Materials Technologies, **5(6)**, 1900981, (2020).
21. R. V. Duraibabu, R. Prithvirajan, M. Sugavaneswaran, G. Arumaikkannu, *Compression behavior of functionally graded cellular materials fabricated with fdm*, Materials Today: Proceedings, **24**, 1035–1041, (2020).
22. A. Garland, G. Fadel, *Design and manufacturing functionally gradient material objects with an off the shelf three-dimensional printer: Challenges and solutions*, Journal of Mechanical Design, **137(11)**, 111407, (2015).
23. J. Wang, S. Mubarak, D. Dhamodharan, N. Divakaran, L. Wu, X. Zhang, *Fabrication of thermoplastic functionally gradient composite parts with anisotropic thermal conductive properties based on multicomponent fused deposition modeling 3D printing*, Composites Communications, **19**, 142–146, (2020).
24. X. Zhang, J. Wang, T. Liu, *3D printing of polycaprolactone-based composites with diversely tunable mechanical gradients via multi-material fused deposition modeling*, Composites Communications, **23**, 100600, (2021).
25. N. Palić, V. Slavković, Ž. Jovanović, F. Živić, N. Grujović, *Mechanical behaviour of small load bearing structures fabricated by 3d printing*, Applied Engineering Letters : Journal of Engineering and Applied Sciences, **4(3)**, 88–92, (2019).
26. B. Saleh, J. Jiang, R. Fathi, T. Al-hababi, Q. Xu, L. Wang, D. Song, A. Ma, *30 Years of functionally graded materials: An overview of manufacturing methods, Applications and Future Challenges*, Composites Part B: Engineering, **201**, 108376, (2020).
27. I. Buj-Corral, A. Bagheri, A. Domínguez-Fernández, R. Casado-López, *Influence of infill and nozzle diameter on porosity of FDM printed parts with rectilinear grid pattern*, Procedia Manufacturing, **41**, 288–295, (2019).
28. K. D. Nguyen, C.-L. Thanh, H. Nguyen-Xuan, M. Abdel-Wahab, *A hybrid phase-field isogeometric analysis to crack propagation in porous functionally graded structures*, Engineering with Computers, (2021).
29. P. M. Ramteke, S. K. Panda, N. Sharma, *Effect of grading pattern and porosity on the eigen characteristics of porous functionally graded structure*, Steel and Composite Structures, **33**, 865–75, (2019).

Development and investigation of new special steel

Argirov Christo, Kalchevska Kamelia
Institute of metal science, equipment and technologies „Akad. A. Balevski" with hydro and aerodynamics centre, Bulgarian Academy of Sciences, Sofia, Bulgaria
E-mail: h.argirov@ims.bas.bg; kami@ims.bas.bg

ABSTRACT: *New special high nitrogen steel used in arms industry is developed. The new steel and technology of its production are developed on the basis of the metallurgy under pressure. The mechanical properties by the results of the short-term strength and notch-impact strength tests are determined. The new steel has higher mechanical characteristics in comparison with conventional nitrogen free analogue. Non-destructive control is carried out. Dense structure without defects is established.*
KEYWORDS*: HIGH NITROGEN SPECIAL STEEL, MECHANICAL PROPERTIES, NON-DESTRUCTIVE TESTING*

1.INTRODUCTION

One of the directions to solve the strategic task of extending the working cycle of industrial machines, tools, etc., is their replacement with such produced of new or improved materials with enhanced exploitation characteristics. As is well known the qualitative metallurgy is metallurgy of the qualitative steels and alloys.The qualitative metallurgy allows inventing new or improved present steels and alloys with special properties and lowering costs of materials and energy. In this way an indirect beneficial environmental effect will be also achieved. The new steels and alloys should possess the necessary complex of mechanical and physical properties and should be superior to the properties of conventional steel brands. Due to the enhanced mechanical and physical properties on the one hand, and the lower costs for materials and energy on other, the steels have a resource for long term operation with reduced production costs. Thus improving the quality of the steels by means of invention of a complex of enhanced mechanical and physical properties at lower production costs ensures the long time operational resource of the products in which the steels are used. All this results have both economic and environmental impact.

Metallurgy under pressure is one of the areas for development of the qualitative metallurgy. This is a method for obtaining of new steels and alloys under pressure above atmospheric pressure.The Institute of metal science, technologies and equipment with hydro and aerodynamics centre "Akad. A. Balevski" to Bulgarian Academy of Sciences (IMSTCH-BAS) has created theoretical grounds in the field of alloying with superequilibrium nitrogen concentration and development of new steel grade-high nitrogen steels and technologies for their production by the methods of the metallurgy under pressure. The Institute has capabilities and years of experience gained in the field of this method. Using the available laboratory facilities in combination with the scientific and technologic potential of the researchers, various new steel brands and technologies for their production were developed. In the basis of the our technological concepts the original Bulgarian methods of Counter pressure casting (CPC) and Electroslag remelting under pressure (ESRP) are incorporated, and also the our knowledge of the processes of nitrogen alloyed. The main advantages of CPC and ESRP for steels production and their alloying with nitrogen include: uniform nitrogen distribution within the ingot since nitrogen is introduced in the liquid bath that is intensive stirred and homogenized; possibility of precise adjustment of the nitrogen concentration; replacement of the expensive alloying elements, such as nickel; smooth and uniform filling of the mould with melt; because of the technological pressure qualitatively new ingots were produced in comparison with those produced upon conventional casting methods: with improved structure, high density and smaller raiser; versatility in obtaining different brands of alloyed steels, especially in combination with ESRP. A number of steel brands with increased nitrogen concentration have been developed in IMSTCH-BAS: high-speed steels, hot-die, cold-die, structural, etc. It was proven that the high-nitrogen steels obtained 30% to 150% higher mechanical parameters in comparison with nitrogen-free steels. Thus the cutter instruments made of the high-nitrogen steel type W6N2Mo5 (analog to W6Mo5, according to DIN S 6-5-2) were characterized by 38% to 100% higher exploitation parameters [1].

At present in arms industry steel 32 NiCrMo 14 5 of type (DIN 1.6745) is widely applied. In the Institute of metal science, equipment and technologies „Akad. A. Balevski" with hydro and aerodynamics centre, Bulgarian Academy of Sciences was carried out investigations to develop original special nitrogen constructional steel 30Cr2Ni2MoN2V [2] of the class of conventional steel 32 NiCrMo 14 5. The new steel and technology of its production are developed on the basis of the metallurgy under pressure. Steel 30Cr2Ni2MoN2V is alloyed with super equilibrium nitrogen quantity while the established by us nitrogen equilibrium concentration is 0, 0465 %. Testimonial investigations of the new special nitrogen steel of 30Cr2Ni2MoN2V mark are carried out. Hopeful experimental results in the process of initial investigations were obtained. Basic mechanical properties [3], dynamical cracking resistance [4], behaviour of the steel at lowered temperatures [5] and others are investigated. In result of these investigations is obtained that the new special steel has higher mechanical characteristics in comparison with conventional nitrogen free analogue 32 NiCrMo 14 5 and does not require antiflake heat treatment [6] – a long and expensive technological operation. To prove the consumer qualities of special nitrogen steel 30Cr2Ni2MoN2V and to determine the production potentialities of steel products, some specific researches, such as short-term mechanical properties and non-destructive testing are carried out.

Purpose of the present work is carried out of of some specific investigations of new special nitrogen constructional steel 30Cr2Ni2MoN2V.

2.EXPERIMENTAL

For the purpose of the our experiment on industrial units induction furnace IFP-05 and installation for Electroslag remelting under pressure ESRP-2 steel ingots are produced of 30Cr2Ni2MoN2V mark and of nitrogen free analogue steel 32 NiCrMo 14 5 for comparative investigations (Table 1). According to developed by us new technology for production of special nitrogen steel follows plastic deformation-forging on radial-forge machine SHL 55 up to a diameter 120 mm and length 2000 mm.

The mechanical properties are determined by the results of short-term strength and notch-impact strength tests. The tensile strength tests (Rm, MPa) are carried out according to BS EN 10002-1:2000 on standard samples by a diameter 102 mm and length 50 mm (A5-specific elongation, %; Z-reduction of area, %; HB-Rockwell hardness). The notch-impact strength tests to Sharpie (KCV, MJ/m^2) – on standard samples by section 10x10 mm to BS EN 10045-1:2001 at temperatures 20^OC and 350^OC.

Non-destructive investigations are carried out in the Laboratory for non-destructive testing in IMSET with HAC-BAS. License I-1193 registration number 04328 for using of ionizing ray sources for scientific and economic purposes. Non-destructive control with radiation methods and with roentgen defectoscope of type 200/5 model MXR-200. Technical parameters: spot focus 2,45x2,80 mm; anode current 5 mA; tension 180 kV at measured equivalent dose 0,210 mSv with tapping ± 0,8 %. Work conditions and reading of the roentgenograms are conformity with Standards BDS EN ISO [7].

Point of the non-destructive testing: Roentgen (X-ray) or Gamma rays are using in the radiation control methods. They penetrate across optical untransparent bodies and operate over photographer's films similar to light rays. Under their operation some substances like for example Zink sulphide, shining (luminescence).

In the roentgen graphic control the radiation source (Roentgen pipe) is placing at a certain distance from object so as the rays to be direct perpendicularly on the axis. On the contrary side Roentgen film is settings. In the irradiation time (X-ray treatment) the film is situated under action of rays in the course of determinate time named exposition. Follows removal of the film in dark from the cassette, development and fixing in order to obtaining a steady photographer's picture. As a result on the section of the investigated object on separate places the picture is with irregular degree of tarnish. Rays who fall into film after passing through a defect are absorbing to a smaller degree in comparison with the rays passed through dense metal. First rays cause stronger darkening of determinate section of the film[8, 9].

3.RESULTS AND DISCUSSION

The obtained experimental results are submitted in Table 1. The analysis of the obtained experimental results shows that in comparison with nitrogen free steel 32 NiCrMO 14 5 the investigated nitride ingots have higher values of yield strength R_{O2} and Rm, MPa at room and at the increased temperature, together with the notch-impact strength at 20^OC. All ingots, with exception of nitrogen free ingot Nr CPC1, satisfy the technical requirements: R_{O2} > 1000 MPA at room temperature. At the increased temperature values of R_{O2} > 900 MPA have only ingots with nitrogen concentration C_N in wt. % from 0, 07 up to 0,112 % (CPC2; ESRP2).

Table 1. *Short-term mechanical properties*

Nr ingot	Heat treatment		Testing temperature, Ttest = 20^oC							Ttest 350^oC
	T_{hard} ^oC	T_{temp} ^oC	C_N wt %	R_{02} MPa	R_m MPa	A5 %	Z %	HB	KCV, MJ/m^2	R_{02} MPa
CPC1	900	580	0,025	1110	1180	15	64	370	0,753	930
		600		990	1100	15	64	331	0,797	870
CPC2	900	580	0.081	1140	1200	16	60	380	0,600	950
		600		1090	1190	15	62	336	0,757	900
ESRP1	900	580	0,012	1140	1230	15	65	385	0,777	970
		600		1060	1140	16	68	327	0,875	900
ESRP2	900	580	0,074	1060	1160	15	61	385	1,030	900
		600		940	1010	16	69	312	1,380	850
ESRP3	900	550-6h	0,107	1143	1242	15	63	375	0,540	973
		550-12h		1110	1190	15	66	-	0,715	930
		580-6h		981	1079	15	66	-	0,953	833
ESRP4	900	580-12h	0,085	1110	1190	14	64	-	0,785	920
		600-6h		999	1111	16	62	-	0,890	864
	1000	600-12h		1110	1180	15	64	-	0,725	910
		620-6h		1024	1114	16	63	-	0,886	850
32NiCrMo 14 5	860	580		970	1102	16	65	-	0,780	780

With respect to the plasticity and notch-impact strength characteristics the investigated ingots have properties essentially exceeding the technical requirements. Thus the sum of nitrogen and carbon concentration in the nitride ingots was kept in the same limits, as for conventional steel. The best combination of strength (Rm>1000 MPa) and notch-impact strength (KCV>0, 60 MJ/m^2) characteristics is obtained after hardening and tempering at temperatures accordingly 900^{o}C and 550^{o}C, 580^{o}C. After the specified heat treatment all ingots have high mechanical properties. By the methods of non-destructive testing the density of the new special steel 30 Cr2Ni2MoN2V is investigated. It is established dense structure without defects. Difference along the height of ingot is not observed (Figure 1). The dense structure after Electrosalg remelting under pressure is one of the advantages of this process. As is known, this advantage "economizes" the finally technological operation-the plastic deformation.

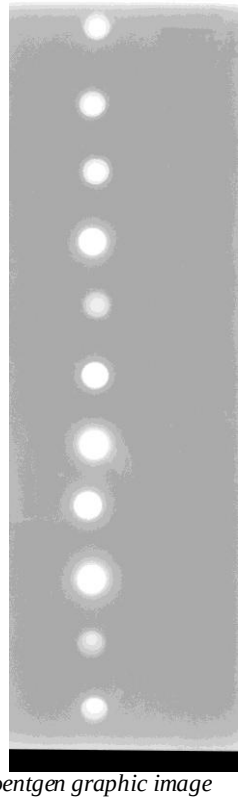


Fig.1. *Roentgen graphic image*

.

4.CONCLUSIONS

Original special nitrogen constructional steel 30Cr2Ni2MoN2V is development. The mechanical properties by the results of the short-term strength and notch-impact strength tests are determined. By the
method of non-destructive testing the density of new special steel along height of ingot is investigated. The dense structure without defects is established. The investigated ingots from special nitrogen steel 30Cr2Ni2MoN2V satisfy the technical requirements: R_{02}>1000 MPa at room temperature. At the working temperature values of R_{02}>900 MPa have the ingots with super equilibrium nitrogen contents in limits from 0, 07-0, 11wt%. With respect to the plasticity and notch-impact strength characteristics the investigated ingots essentially exceed the technical requirements.

REFERENCES

1.Rashev Ts. High nitrogen steels. Metallurgy under pressure.Sofia, Prof. Marin Drinov Publishing House of BAS, 1995, pp.5-9.
2.Patent Russia Nr 1627584: Steel, Argirov Ch. 15. 02. 1990.
3.Davidov Y., Kolev S., Argirov H. Nitrogen influence on mechanical properties of steel for threaded connection elements. International Conference ECF 9: Reliability and structural integrity of advanced materials, 1992, Varna, pp. 1029-1032.
4.Argirov H. Researches on dynamical crack stability of high nitrogen structural steel. Technical Ideas. XLI.2004, 1-2, pp. 106-113.
5.Argirov H. and others. Researches on the behaviour of high nitrogen structural steel at lowering temperatures. Engineering sciences. Year XLII, 2005. 1. Pp. 66-73.
6. Argirov H. Development of new high sensible structural steel without antiflake heat treatment by the metallurgy under pressure. 6th International Conference on HNS 02. Chennai, India. February 21-24.2002. Transaction Indian Institute of Metals. V. 55, 5 October 2002, pp. 489-494.
7. BDS EN ISO 5579:2013 Testing (control) without destruction. Radiographicall testing of metal materials by roentgen and gamma rays using film by roentgen and gamma rays. Basic rules.
8. Mirchev Y., K. Kalchevska, M. Mihovski, A. Tucova. Physical basis methods, materials and means for capillary non-destructive control. 2019. Format 160x230, pp. 140. ISBN 978-619-90662-2-5.
9. Kalchevska K., Y. Mirchev, M. Mihovski. Physical basis, methods, means and technologies for visual-optical and measuring non-destructive control. Sofia, 2020. Prof. Marin Drinov Publishing House of BAS. ISBN 978-619-345-038-0. Pp. 144

Technical requirements for the materials from which clothes for firefighters are made. Types of tests

Ivanov Ivan [1], Nikolova Valentina [2], Liliq Damyanova [3]
Institute of Metal Science, Equipment and Technology with Hydroaerodynamic Center at Bulgarian Academy of Sciences, 67 Shipchenski Prohod Street, 1574 Sofia, Bulgaria[1,2,3]
Email itoivanov@abv.bg[1],valya_g@abv.bg[2], lilydamianova@gmail.com[3]

Abstract: *The report examined the technical requirements for materials from which firefighters' clothing is made and the types of testing of the materials from which the specialized protective equipment for the protection of firefighters, for neutralizing and eliminating threats and their follow-up to incidents at critical infrastructure sites are made.*

Keywords: *CRITICAL INFRASTRUCTURE SITES, FIREFIGHTERS' REMEDIES*

1. Introduction

The modern development of technology predetermines the use of heterogeneous substances and materials in the production of clothing for firefighters.. Many of them, according to their physico-chemical properties, are combustible, explosive and toxic. The requirements for specialized protective equipment for the protection of firefighters involved in accidents and their neutralization of their consequences are determined by the physico-chemical properties of the material from which they are made. The purposes of the garments are to protect the body of the firefighter to the maximum extent possible, to have minimal movement restrictions and to be of minimal weight.

Although there are no universal protections to protect, the research is aimed at universalising them in terms of activities in which to use them. Modern protective garments are designed and made, identifying the areas of application. . [1,2,3,4,5,6]

Clothes for firefighters are made of multi-layer fabrics or one-layer fabrics. In the first option, where they are multi-layered, the surface layer is in direct contact with the environment in which it is used and therefore has the greatest requirements, such as:

- be in combustible;
- be antistatic;
- do not leak water and air/gases;
- be dielectric;
- to resistant to chemicals;
- be mechanically durable and not change its characteristics over time.
- have a minimum weight;

2. Technical requirements for materials for surface layer textiles from which garments for firefighters are made

Protective clothing for firefighters is a specialized personal protective equipment, providing protection of the torso, neck, hands and feet of the firefighter. [7]

The type of clothing of the firefighter is determined depending on the specific incident in which it will be worn. For this, the top layer of clothing must have technical parameters that must protect the remaining layers of clothing and body from the harmful environment.

In all cases of use, two are the main characteristics that are basic and mandatory, in the case of different types of clothing for firefighters, respectively, and to the surface layer of clothing: to be non-combustible (its combustion behavior) and to be mechanically durable (to withstand mechanical wear and not to change its characteristics).

2.1 Surface layer of textile combustion behaviour

To determine the heat and behaviour of the fiery impact of the surface layer of textiles and, where appropriate, to be tested.

The purpose is to determine the moment of ignition by means of tests, the samples being placed vertically, due to their faster ignition and spread of combustion.

Using a test, the properties of textile fabrics in contact with fire shall be assessed, to what extent they are retained and for how long [8,9].

The test shall be carried out at a defined minimum ignition time and a well-formed flame from a burner which can be adjusted in the range of 10 mm to 60 mm. For combustion, liquefied gas or butane/propane mixtures are used in the burner.

The working position of the burner shall be at the front, below the test specimen, so that it is in a plane through the vertical centreline of the specimen and perpendicular to its own surface with its longitudinal axis inclined below 30o towards the vertical lower edge of the test specimen. The distance between the tip of the burner stabilizer and the lower end of the test image is required to be 20 mm ±1 mm.

Adjust the flame after ignition and heat for two minutes. The height of the flame shall be 40 mm ± 2 mm and the measurement shall be from the top of the burner stabilizer to the extreme point of the yellow part of the flame, looking against a dark background. The height of the flame shall be tested before the samples are tested.

To measure the combustion time, a relay device is used to control and measure the flame application time with the possibility of adjusting 1 second with an accuracy of 0,2 seconds. In order to measure the time after ignition, three relays with readings up to 0,2 seconds are required.

A device starts automatically at the moment the flame is sharpened or stopped, stopping manually.



Figure 1 - Apparatus for conducting tissue combustibility tests

The apparatus for conducting the combustibility test of tissues is shown in Fig.1. It consists of a performance reporting computer, a textile sample frame, a burner, ignition time reporting relays and burner reading markers in the vertical. The listed deer are placed in an isolated environment after their preliminary conditioning and tempering.

For textile testing, 12 samples/samples are taken.

The samples are tested in a vertical direction, with the outer layer directed to the flame source.

The samples shall be the dimensions (200 mm ± 2 mm) x (80 mm ±2 mm) which are tempered in advance at a temperature of 20 ^{0}C ± 2 ^{0}C and a humidity of 65 % ±5 % for 24 hours. If testing is

not carried out immediately after conditioning, the samples shall be placed in a sealed container and testing must be initiated within 2 minutes of being removed from the conditioning atmosphere.

Test procedures:

– if a specimen ignites within 1 second, cary not burning '0' is recorded and the test is repeated by 1 second in the duration of application of the flame;

-if there is no ignition within 20 seconds, repeat the test again with 20 seconds of ignition time. Testing continues until 5 examples of combustion and 5 examples of non-combustion appear.

The maximum time of application of the flame is 20 seconds.

The samples shall be tested by ignition and at the lower end.

The results obtained from the test from all the ignition and ineeding times recorded shall be calculated the average time at which the specimen is ignited. The purpose of these tests is to determine the average combustion time of the test specimen, which is the minimum flame application time, in order to reproduce continuous combustion under certain test conditions calculated to the nearest second. (An example of an average time of 4.2 seconds is taken from all circumcised time of 4.2 seconds).

The average time is the limit between burning and burning the specimen. Both types of behavior can be observed by tiping the pattern the flame is applied just as long as the average time. Testing of non-combustible materials is not appropriate, as is the use of materials that have only limited combustion. The results obtained are in the column "un ignited at 20 seconds application of flame- "lightness of ignition".

After determining the mean ignition time, another important indicator is the 'flame propagation time' – the time it takes for the flame on the burning material to travel a certain distance under certain test conditions [10]. Three devices (relays) are used to read the time. Relays reading to within 0.2 seconds. Measure the flame propagation times, starting the devices simultaneously when applying a flame and stopping automatically when the individual marker threads are damaged/destroyed.

The method is designed to test flammable materials that support the flame when ignited. In this type of material, this method is accurate to the nearest second.

The precision of the results depends to a large extent on the type of material to be tested. When testing system materials, ignition and combustion of the specimen shall be reported.

The procedures described with regard to the determination of the average ignition time and the time of spread of the flame are used in tests of textile fabrics for clothing, a procedure for determining combustion behaviour [11,12,13].

Tests of samples have been carried out in an accredited test laboratory - "TEX CONTROL" Ltd- Bulgaria, Gabrovo.

The apparatus on which the tests were carried out in the accredited laboratory is SHIRLEY FLAMMABILITY TESTER mode; M233B - Fig. 1. The results of the tests carried out on five samples of different materials with different technical characteristics are shown in Table No1 and Fig. 2.

Table № 1

Type of material	Mass per unit area [g/m^2]	Mean ignition time of vertical-female samples [s]	Quantitative analysis	Weave
META ARAMID FLAME- PRO, after anticomar apreture and after sanfor	251,98	0/0/0	49/49 /(2 -4) viscose/aramid/antistatic	keper
KORDURA 5 color print with non-combustible smear, TL 8305-0278/from TMN - Austria/	249	>20		keper
REGATTA,T.P.304, after sanfor	330	0,4	100% cotton	satin
FRESCO after softening and sanfor	163	0/0/0	((49/49 /(2 -m4)± 2 viscose/aramid/antistatic	
SAMPLE	261	0/0/0	93% Nomex, 5% Kevlar, 2% antistatic	

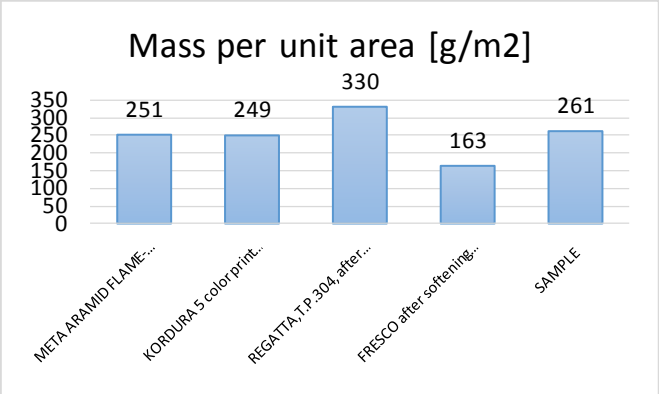


Fig.2 Mass of test samples

Table №2

Type of material	Flame propagation time of vertically located samples when igniting: ground -in length (first, second and third marker threads) [s]		Weave
META ARAMID FLAME-PRO, after anticomar apreture and after sanfor	first marker thread:0 second marker thread:0 third marker thread:0		keper
KORDURA 5 color print with non-combustible smear, TL 8305-0278/from TMN - Austria/	first marker thread:0 second marker thread:0 third marker thread:0		keper
REGATTA,T.P.304, after sanfor	first marker thread:0 second marker thread:0 third marker thread:0		satin
FRESCO after softening and sanfor	at 5 s burning≤1 smoldering≤5	at 15 s burning≤0 smoldering≤5	
SAMPLE	at 5 s burning≤4 smoldering≤5	at 15 s burning≤0 smoldering≤5	

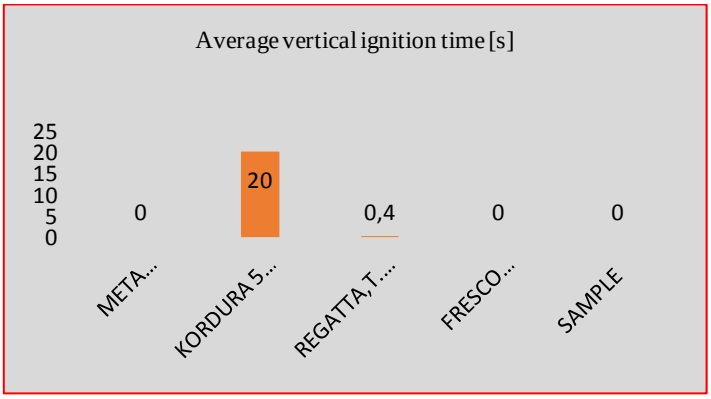


Fig. 3 Average ignition time of samples

2.2. Determination of the rupture of the surface layer.

To determine the strength of the raking, the surface layer of textiles shall be tested. No change in size should be observed after testing, use and cleaning of the material for a surface layer for protective clothing.

Permissible changes of a surface layer shall not exceed ±3 % for fabrics and ±5 % for knitted material and non-woven fabrics.

The method by which the study is carried out [14] - STRIP refers to the determination of the maximum breaking force of fabrics when the force is located on the tested pattern of textiles, both on the basis and in wee. The method is not applicable to fabrics of elastic fabrics, geotextiles, non-woven fabrics, coated fabrics, woven fabrics of glass fiber and carbon fiber fabrics.

In tests, a constant rate of extension machine is used. The tensile test machine shall be fitted with one gripping jaw which is stationary and another which is moving at constant speed during the test.

Tests of samples have been carried out in an accredited test laboratory - "TEX CONTROL" Ltd - Bulgaria. Gabrovo.

The apparatus for which the tests were carried out in an accredited laboratory is Zweigle F 427, shown in Fig.№ 4,



Fig. 4 tensile testing equipment

The results of the tests carried out on five samples of different materials have different technical characteristics are shown in Table № 3

Таблица №3

Type of material	Power of rationing basis [N]		Power of rationing Weft [N]		Quantitative analysis
	test	norm	test	norm	
META ARAMID FLAME- PRO, after anticomar apreture and after sanfor	31,9	35	35,2	35	49/49 /(2 -4) viscose/aramid/ antistatic
KORDURA 5 color print with non-combustible smear, TL 8305-0278/from TMN - Austria/	273,3		252,3		
REGATTA,T.P.304, after sanfor	116,8	110	82,8	80	100% cotton
FRESCO after softening and sanfor	27,9	12	25,2	23	(49/49 /(2 -m4)± 2 viscose/aramid/ antistatic
SAMPLE					93% Nomex, 5% Kevlar, 2% antistatic

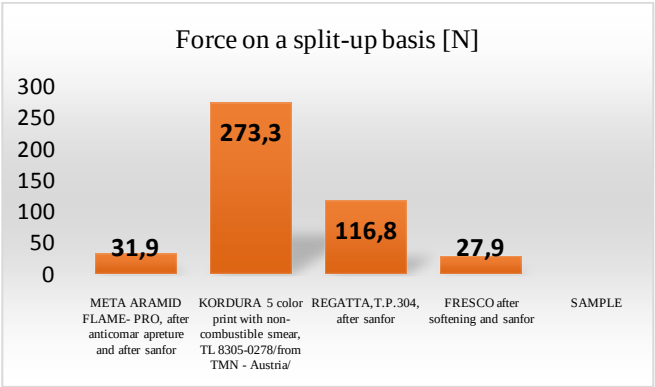


Fig.4 Sampling force

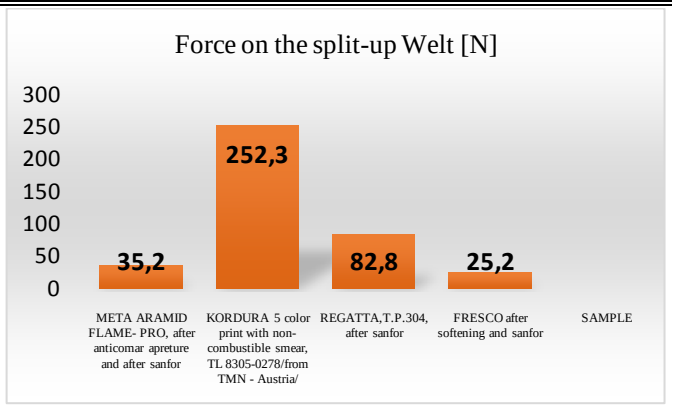


Fig.5 Sampling strength

When testing the external material after pre-treatment, its base and weath strands must withstand a rupture force of ≥ 30 N to meet the requirements for use in clothing for firefighters. [1]

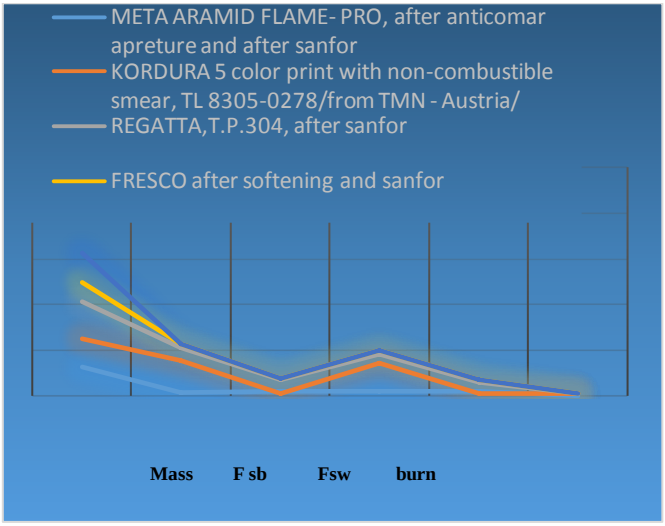


Fig.6 The comparative results of the test specimens are

From the results obtained described in table No 2, with average test data of five counts, the following conclusions may be drawn:

-Further treated textiles in order to improve its fire resistance to fire, greater resistance to fire and non-flammability is established by not igniting for 20 seconds:

-With the additional treatment, sample screed № 2 (Cordura 5) has a mass of a single area of 249 g/m^2, is almost as raw samples of material № 1 (meta aramid) with a mass of 251 g/m2 (Fig. 2)

- Samples of synthetic composition are ignited immediately while organic materials are recorded at a time of 0,4 s (Fig. 3)

- Some synthetic materials have higher indicators of mechanical resistance than organic materials.

- the type of material has importance - its chemical composition, the goal is to achieve a combustion-resistant textile, non-growing combustion with a low heat transfer coefficient and a reduced mass of edenic area;

-The type of textile braid in the tested robes is relevant, the results show that the tper weave is more resistant to flame spread than an satin braid.

- It is apparent from the tested samples that melt-resistant textiles are made of natural materials, but are more unstable to spread fire than synthetic products with additional processing smear.

- Cordura-branded sample tested sample has the highest performance in terms of base and weaning strength, which shows its mechanized durability and strength.

3. Conclusions

Following the tests carried out on five samples of textiles of different types, the following conclusion may be drawn:

- there is a tendency to achieve material that can withstand a longer fire time and temporarily reduce the mass of a single area.

Depending on the material, a type of textile design for a surface layer is more appropriate to use only in certain activities, examining combinations of new materials in a different weave and further processing until the goal of making a fabric resistant to a wide range of harmfulness, with minimal weight and without creating movement restrictions, with a sufficient degree of mechanical durability.

The results are aimed at the implementation of Work Package 2 "Intelligent Security Systems" of project BG05M2OP001-1.002-0006 "Construction and development of the Competence Center "Quantum Communication, Intelligent Security Systems and Risk Management (Quasar)", which has received funding from the European Regional Development Fund through the Operational Program "Science and Education for Smart Growth" 2014-2020.

4. References

1. Yaneva S. Ergonomic requirements for the individual equipment of the antiterorist used in critical infrastructure sites. international shentifik technical conference. Technique. Technology. education. saphetti'17, prokeding, ise 1 (1), suffia, English 2017, volume 1, militaris syansis an national securititis, shentific technical union of mechanical enguinering "industry-4.0" yun 2017, isn 2535-0315(print), isn 2535-0315(online), p. 70-71

2. Yaneva S., Materials used in the means of individual ballistic protection. Analysis, Advantages and Disadvantages, International Scientific Conference "Asymmetric Threats, Hybrid Wars and Their Impact on National Security", March 16, 2018, New Bulgarian University, Department of National and International Security, Proceedings of Scientific Papers, Publisher: NTS in Mechanical Engineering "Industry-4.0", ISBN 978-619-7383-09-6, p. 439-447

3. Yaneva S., Tumbarska A. Petkov S., Types of bulletproof vest. Classification, VI International Scientific and Technical Conference “Engineering. Technologies. Education. Security” 30 May – 02 June 2018, Veliko Tarnovo, Proceedings, Volume I. Military Science and Security. Year II, Issue 1 (4), June 2018, ISSN 2535-0315 (Print) и ISSN 2535-0323 (Online), p.94-96. Published: INTERNATIONAL SCIENTIFIC JOURNAL “SECURITY & FUTURE”, Year II, Issue 1/2018, June 2018, ISSN 2535-0668 (Print) и ISSN 2535-082X (Online), p.43-45.

4. Yaneva S. Testing and evaluation of the resistance to puncture and the protective properties of flexible ballistic panels of bulletproof vests, 20th International Conference “Materials, Methods & Technologies”, 26-30 June 2018, Elenite Holiday Village, Bulgaria. Published: JOURNAL OF INTERNATIONAL SCIENTIFIC PUBLICATIONS “MATERIALS, METHODS & TECHNOLOGIES”, Volume 12, 2018, ISSN 1314-7269, 6 Sep 2018, p. 209-223,

5. S. Yaneva, STAB RESISTANCE OF BULLETPROOF VESTS. A CONCEPTUAL MODEL OF TEST BENCH, Proceedings of VII International BAPT Conference “Power Transmissions 2020”, 10–13.06.2020 Borovets, Bulgaria, Publisher: Scientific-Technical Union Of Mechanical Engineering - Industry 4.0, ISBN 978-619-7383-18-8, p.122-126

6. S. Yaneva, BALLISTIC RESISTANCE OF BULLETPROOF VESTS LEVEL IIIA. DEVELOPMENT OF TESTING METHODOLOGY, Proceedings of VII International BAPT Conference “Power Transmissions 2020”, 10–13.06.2020 Borovets, Bulgaria, Publisher: Scientific-Technical Union Of Mechanical Engineering - Industry 4.0, ISBN 978-619-7383-18-8, p.127-131 (WEB OF SCIENCE) Published in: Issue: MATEC Web of Conferences, Volume 317, (2020), Article Number: 06003, 7th International BAPT Conference “Power Transmissions 2020”, Borovets, Bulgaria, June 10-13, 2020, D.P. Karaivanov (Ed.), eISSN: 2261-236X, Published online: 03 August 2020, p.1-5

7.BDS EN 469: 2021 Protective clothing for firefighters – fulfilling requirements for protective clothing for fire extinguishing.

8. BDS EN 1103:2006: Textil. Fabrics for clothing. Detailed procedure for determining combustion behaviour

9. Average ignition time of vertically positioned samples when igniting: ground /lower edge - length and/or width - BDS EN ISO 6940:2006

10. BDS EN ISO 6941 - Textile fabrics. Combustion behavior. Measuring the spread of flame in vertically decomposed robes.

11. BDS EN 1103:2006: Textil. Fabrics for clothing. Detailed procedure for determining combustion behaviour

12. Total mass per unit area (coated textiles) - BDS EN ISO 2286-2:2000, method A

13. Maximum force to break using STRIP method - base - weed - BDS EN ISO 13934-1:2013

1.1.30 Power of development (tongue-shaped specimen) - base - weed - BDS EN ISO 13937-4:2002

14. Number of threads per unit length - base - weak - BDS END 1049-2:2002, method A .

Physicochemical and technological researches of marls from the area of the village Lovets related to the production of the new "Yellow paving stones"

Lyuben Lakov, Gergana Mutafchieva*, Gabriel Peev, Mihaela Aleksandrova, Bojidar Jivov
Bulgarian Academy of Sciences , Institute of Metal Science, Equipment, and Technologies with Center for Hydro- and Aerodynamics "Acad. A. Balevski", cl.creativeline@gmail.com

Abstract: *Due to force majeure circumstances, new researches of marls from the Alexandra deposit to the village of Lovets (Shumen region) were carried out to replace the marls from the village Svetlen (Targovishte region), which are part of a plastic mass for the production of large, fine-ceramic parts (yellow paving stones) from peturgical phases. Marls are characterized in terms of mineral and chemical composition. Their properties, characterizing them as a ceramic raw material, have been determined. Three test masses with a chemical composition similar to the one with the participation of marls from the village of Svetlen were developed. The test specimens are characterized in terms of sintering and strength characteristics. It has been established that the marls can be used to repla ce the marl from the village Svetlen in the composition of the plastic fine-ceramic masses for the production of yellow pavers.*
Keywords*: MARBLE CLAYS, NEW YELLOW COATS, PHYSICOCHEMICAL STUDIES OF MARBLE*

1. Introduction

Due to the bankrupt of the company "Rodna Industria" Popovo, using the concession of the marl deposit in the village Svetlen in obligations to the state, insolvency and lack of prospects for future cooperation, it was necessary to urgently conduct current research to find new alternative raw materials.

2. Representation

Both the marl from the village Svetlen and the marl from the village Lovets are used for coarse ceramic products - bricks. As marls are suitable for the production of high quality majolica tiles, they can easily be used as a raw material for the production of fine ceramic products, because clay marls contain a larger amount of fine fractions than typical brick clays [1]. The carbonates in the marls are more evenly distributed. Table 1 shows the chemical composition of marl from the village Lovets, and Figure 1 shows a radiograph of the raw material and the content of mineral phases in it. Table 2 presents the grain size distribution in% by weight.

Table 1: *Chemical composition of marl clay from the Alexandra deposit, Lovets village*

Composition	Quantity %
Na_2O	0,7
MgO	2,24
Al_2O_3	11,36
SiO2	35,19
$P2O_5$	0,1
K2O	2
CaO	19,58
TiO_2	0,47
MnO	0,11
Fe_2O_3	4,85
LOI	23,21
Σ	99,82
Cu	0,06
Zn	0,073
Sr	0,053

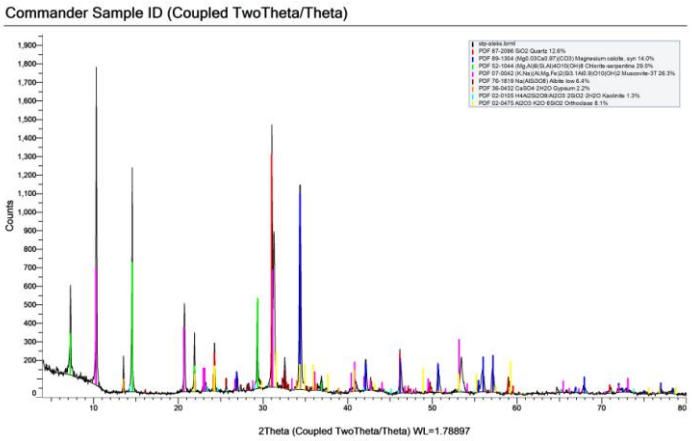


Fig. 1. *Phase analysis of dried marl clay from the village of Lovets at t =1140°C and retention at a final temperature of 80 minutes.*

Table 2: *Grain size distribution of marl clay as a percentage of particle size.*

Grain size distribution	Weight %
Faction under 0,005	45
Faction 0,005 - 0,05	42
Faction over 0,05	13

According to the standards, the studied clay belongs to the marls of group III - acidic below 15% Al_2O_3 high-carbonate, over 17 - 18% alkaline earth oxides and high content of coloring Fe_2O_3 - over 3%. According to the classification of Sitin, the clay marl used by us from the area of the village Lovets, the amount of alkaline earth oxides is 21.82% by weight. This implies a relatively narrow firing interval and difficulty in obtaining fine ceramic products. The DTA curve of marl showed a characteristic endoeffect at 800°C associated with the decomposition of $CaCO_3$ and $MgCO_3$. The weight reduction is 22.57%, which coincides with the determined by chemical analysis A.L.(annealing losses). 23.71%. From the DTA curve shown in fig. 2, it has surprisingly been found that the melting interval begins with the appearance of small amounts of liquid phase as early as approximately 1000°C before the actual melting point at 1137-1140°C. This suggests that a practical temperature regime for marl firing could be established.

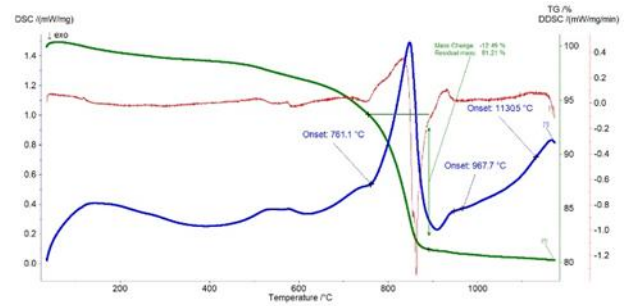


Fig. 2: *DTA-DSC analisys of the test samples*

X-ray phase analysis shows that marl contains, in addition to calcite ($CaCO_3$), chloride, mica such as musk quartz, feldspar, plagioclase, gypsum and kaolin. The content of clay substance is in accordance with the fractional composition (fraction below 0.005 - 45%) fig. 1.

Marl has the following properties, characterizing it as a ceramic raw material:

- Normal molding humidity - 20.5%;
- Plasticity according to Pfefferkorn - 29%;
- Critical humidity - 17.3%;
- Coefficient of sensitivity to drying - 0.18.

The clay marl used in plastic plastics has a favorable high critical humidity and is slightly sensitive to drying. This is in accordance with its mineral, chemical and fractional composition, which determines a simplified drying regime and the possibility of forming according to the classical technologies of ceramic technology. The recipe composition of the working tables used is presented in Table 3.

Tabl. 3. *Prescription composition of working tables*

Raw materials	Composition of test masses by weight %			
Marl from the village of Lovets	25	30	30	30
Fireclay from marl in the village of Lovets	55	55	60	70
Washed kaolin, dried at 120°C	20	15	10	-

The calculated chemical composition of the test masses is given in Table 4.

Tabl. 4. *Prescription composition of work tables*

Оксиди	M1	M2	M3	M4
Na_2O	0,60	0,66	0,67	0,70
MgO	2,16	2,14	2,14	2,24
Al_2O_3	12,60	13,00	13,10	11,36
SiO_2	41,30	39,98	40,10	37,19
P_2O_5	0,07	0,072	0,73	0,10
K_2O	1,80	1,85	1,90	2,00
CaO	16,70	17,32	19,30	20,58
TiO_2	0,33	0,34	0,34	0,47
MnO	0,10	0,11	0,11	0,11
Fe_2O_3	4,75	4,80	4,83	4,85
A.L.	19,425	20,90	21,00	20,21
Cu	0,05	0,06	0,06	0,06
Zn	0,066	0,069	0,068	0,073
Sr	0,049	0,051	0,052	0,053
	100,00	100,00	100,00	100,00

Slips with a humidity of 60% are prepared from the work tables. The plastic mass for the test samples was obtained by dehydrating the slip in gypsum forms to normal molding humidity, which for all four masses was 22%. The obtained samples from the plastic masses are tiles with dimensions 56.5 x 56.5 x 5.65, dried to a residual humidity of 2-3%.

The properties of the obtained water-dispersed colloidal systems (slips) are presented in Table 5.

Tabl. 5. *Properties of the four slips obtained from clay*

Properties	M1	M2	M3	M4
Liter weight g/l	1490	1485	1480	1492
Viscosity, Pas	2,30	2,25	2,23	2,22
Dry matter in the dispersed system , kg/l	0,80	0,79	0,78	0,77
Sieve residue in the sieve 0.063 mm g / l	0,09	0,10	0,11	0,25

The firing mode is determined by the DTA curve and is as follows: heating rate 3°C / minute; delay at 112°C and 148° C for 30 minutes; retention at 576°C, 687°C and 800°C - 20 minutes and retention at final temperature 1130°C - 60 minutes. The cooling rate is 3°C / minute and a hold at 576°C and 687°C for 30 minutes.

The results of the degree of sintering of the test samples up to 1160°C are presented in Table 6, and the mineral phases in the synthesized mass sample №4 are presented in Figure 3.

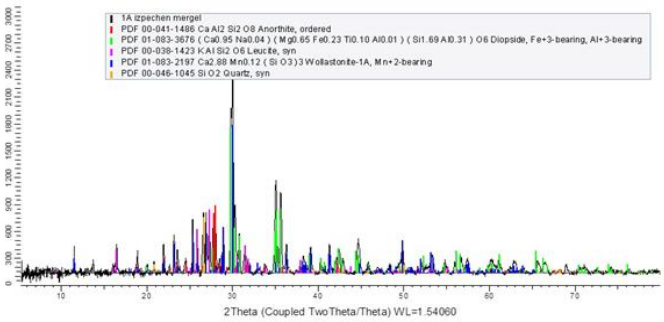
Tabl. 6. *Characteristics and degree of sintering of the test specimens at three temperature processes*

Maca	T°C calcination	contrastility	Water absorption	Appearant density
M1	1000	5,0	22,0	1,70
	1130	7,0	12,0	1,72
	1160	8,0	0,2	1,85
M2	1000	6,5	24,5	1,65
	1130	7,9	0,06	1,67
	1160	melt	0,0	-
M3	1000	6,0	20,2	1,63
	1130	8,0	0,04	1,65
	1160	melt	0,0	-
M4	1000	7,1	14,8	1,80
	1130	8,4	0,02	1,85
	1160	melt	0,0	-

Samples of mass M4 at annealing temperature of 1130°C and mass M1 at annealing temperature of 1160°C are best sintered, in

which the water absorption is 0 and 0%, respectively, and the apparent density of both samples is 1.85 g / cm^3

The higher content of $CaCO_3$ reduces the viscosity of the mass during sintering, respectively the interval of sintering. The M4 mass burns the fastest and at the lowest temperature, which is due to the larger amount of melt formed. At a temperature of 1130°C the water absorption is 0%, but the baking interval - 15/20°C is the narrowest.



Фиг. 3. *Radiograph of a high-temperature synthesized sample of mass №1 shows the presence of peturgical phases anortite and diopside, which predetermine the good physico-chemical and mechanical parameters of the finished products shown in table. 7.*

The strength characteristics of the samples of test masses M1, M2, M3 and M4 are presented in Table 7.

Tabl. 7. *Compressive strength and bending strength of test specimens at different temperatures*

Indicators	M1	M2	M3	M4	T°C firing temperature
compressive strength, MPa	800 1000 1200	900 1100 -	950 1150 -	1000 1250 -	1000 1130 1160
Bending strength, MPa	116 140 460	120 400 -	125 420 -	140 470 -	1000 1130 1160

3. Conclusion

The results of the research confirm the possibility of using the marl from the Alexandra deposit to the village of Lovets, Targovishte district. However, the use of marl clay from this deposit requires a change in the technological process, which is the main goal in the present development.

Acknowledgement

The authors are grateful to the financial support of the Bulgarian National Science Fund at the Ministry of Education and Science, Contract No КП-06-ОПР 03/4 14.12.2018, for carrying out the necessary research.

All equipment and experimental units used in this work was funded by the European Regional Development Fund within the OP "Science and Education for Smart Growth 2014 - 2020", project CoE "National center of mechatronics and clean technologies", № BG05M2OP001-1.001-0008-C08

References

1. Gerasimov, E., Bachvarov, S., at al, "Technology of ceramic products and materials", 2003, Sarasvati, Handbook, ISBN 954-9841-15-4.
2. Berger, I. at al, "Freiformen und freidrehen, Handbuch der keramik, Gruppe ID2.7. Freburg.V. Schmid, 1991.
3. Bachvarov. S., at al, "Guide for laboratory experiments on the silicate technology", Handbook, pp159-192.
4. Lipinski, F. Das Keramische Laboratorium, Verlang Knapp, Halle (Saale), 1969.
5. Callister, William D., D. G. Rethwish., Materials Science and Engineering: an introduction, 8th (Wiley 2009).

Set up for real time capturing of welding parameters

Deyan Gradinarov[1]
Institute of Metal Science, Equipment and Technology with Hydroaerodynamic Center at Bulgarian Academy of Sciences[1]
dgradinarov@ims.bas.bg

Abstract: *It is presented set up for real time capturing welding parameters – voltage, current and temperature in specific points of welding process.*
Keywords*: REAL TIME, REALT TIME CAPTRING, WELDING PARAMETERS*

1. Introduction

According to the modern requirements for low energy intensity and environmental protection and in the context of declining natural resources, scientists, the business, and the society are looking for ways to meet the growing needs of various industries, from optimizing and improving welding methods to adding additional alloying elements for better weldability.

The welding process is used in almost every area of human activity, and the need products of this process is constantly increasing. With the increase of the responsibility of the welded joints, the requirement for welding quality is also increased.

The welding process is performed according to a pre-approved and validated Welding Procedure. This welding procedure sets the welding technology, welding mode, current, voltage, welding speed, wire feed rate, flux used, type, diameter and tip pre-forming of the welding wire, welding and break time, and other parameters on which the quality and reliability of the welded joint depends. Deviating from them, with a high probability, leads to a decrease in the properties of the welded joint, and hence to defects and damage that increases the risk of injuries and endangering human life and negative environmental consequences.

When welding by an operator, due to a number of factors that cannot be avoided, the welder can deviate from the welding procedure, with the welding process being carried out at welding parameters that differ from the procedure. This leads to the presence of defects - gas and slag inclusions, welding cracks, unexpected change of the main metal properties in the surrounding area, etc. The presence of such defects directly affects the exploitation properties of the manufactured parts and elements by reducing their strength, lifetime, reliability, etc. When applied conscientious control, this leads to wastage, cost increases and waste of resources - metal, welding wire, welding gases and energy. In case of unconscious control - to the direct danger of traumatism, accidents, ecological catastrophes, etc., which directly or indirectly affects the society.

Improving the welding process by the real time control of welding parameters compared to those set in the welding procedure reduces drastically the possibility of defects and thus gives economic and environmental advantages by reducing wastage and consequently consumption of metal, gas, electricity and water to reducing emissions.

The results of the research show that there are numerous studies on the methods and technologies for monitoring and control of the welding parameters, the influence of the parameters on the exploitation properties of the welded elements, the quality determination of the welded joints.

It is studied the influence of the welding parameters in various welding processes and their impact on the quality and performance of the welded joints [1,2,3].

One of the current problems of modern material science is methods for increasing the life cycle of parts with welded joints, which must have both high hardness and strength and low internal stress. It is studied the impact of welding parameters on the morbidity of welded joints [4,5].

There are known studies on welding process optimization methods by control of welding parameters [6,7,8].

There are studies on welding parameters control and welding optimization [9,10] as well as methodologies for determining the parameters in welding processes [11].

There are developed welding parameters parameter control systems [12,13,14].

The analysis of our well-known sources does not give enough clarity to the question: what impact the welding parameters have on the performance of the welded joints and what methodologies should be used to improve the quality of the process.

This leads to the need to acquire new fundamental knowledge about the possibilities, means and rate of improving the quality of the welding processes by real time control of parameters.

A thorough study and determination of the influence of welding parameters on the quality of the process and analysis of the possibilities for quality improvement through real time control is also needed.

2. Set up for real time capturing of welding parameters

The set up has two main parts – welding equipment and measuring equipment. The welding equipment consists of welding torch, which is mounted on mechanical grip. The mechanical grip fixes the torch in one position and removes fluctuations from welder's movements. The mechanical grip is mounted on welding tractor, which moves along and over the welded elements with constant speed. Welded elements are placed on welding table. Next to the welding table are placed the power source that feeds the torch and gas bottle that protects the joint. The measuring equipment consists of capturing module Lincoln Arc Tracker. Arc tracker captures welding current and voltage. It is connected to WiFi Router that transmits the data to laptop. On tripod is placed pyrometer IL 92 that measures contactless the temperature in one point next the welding joint. The pyrometer is connected via USB cable to the laptop. The pyrometer is placed on 1,5 m distance from the measured point. It is developed program with Matlab for capturing the temperature from the pyrometer. Temperature of the process is measured with 8-channel contact thermometer Spider 8. K type thermocouples are connected to the Spider 8 and set in 8 point next the welding joint. Thermocouples are welded to the welded elements. The Spider 8 is connected to the laptop with UBS cable. Temperature is captured by Spider 8 with software Catman.

Il 92 pyrometer was chosen to perform the experiment, which has wide temperatures measurement range, including liquid metals, can be freely measured. The excellent distance / measured spot ratio of 50:1 allows long-distance measurement of small objects, as well as in extreme conditions, e.g.: in the furnace. The characteristics of the device are: measuring range: -50 to 2200^{o}C; accuracy of the device ± 2%; reaction time - 150ms; spectral range - 8-14µm.

The set up functionality is verified with experiment with the following parameters:

- welding current – 210A
- welding volatage – 25V;
- η of the welding source – 0,8;

- welding power – 4200J/s;
- welding speed – 50cm/min;
- welding steel plates 50x5x200mm.

The real time data sequences are shown as follows – welding current on Fig.1 and welding voltage on Fig. 2 from Arc Tracker, temperature from Pyrometer on Fig.3 and from the contact thermometer on Fig.4

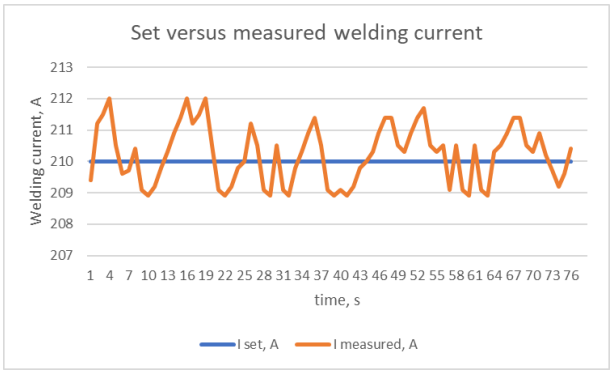


Fig. 1 *Measured welding current by Arc Tracker.*

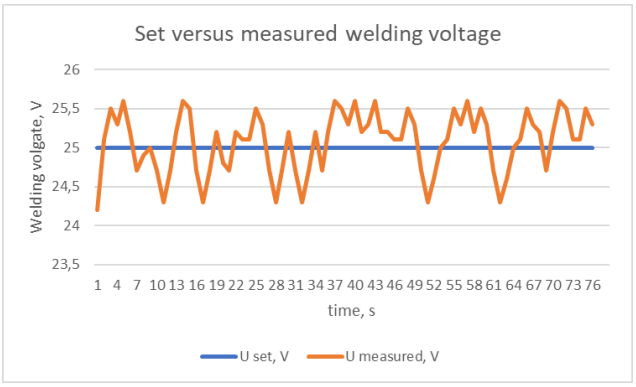


Fig. 2 *Measured welding voltage by Arc Tracker*

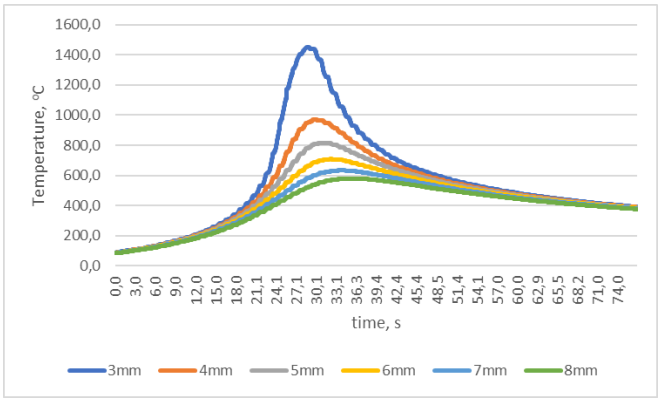


Fig. 3 *Measured contactless temperature by the pyrometer.*

3. Conclusions

It is developed set up for real time capturing of welding parameters – welding current and voltage, contact and contactless temperature in fixed specific points of interest.

Acknowledgments

This work was made possible by a project KP-06-N37/31, funded by the NSF.

All equipment and experimental units used in this work was funded by the European Regional Development Fund within the OP "Science and Education for Smart Growth 2014 - 2020", project CoE "National center of mechatronics and clean technologies", № BG05M2OP001-1.001-0008-C08

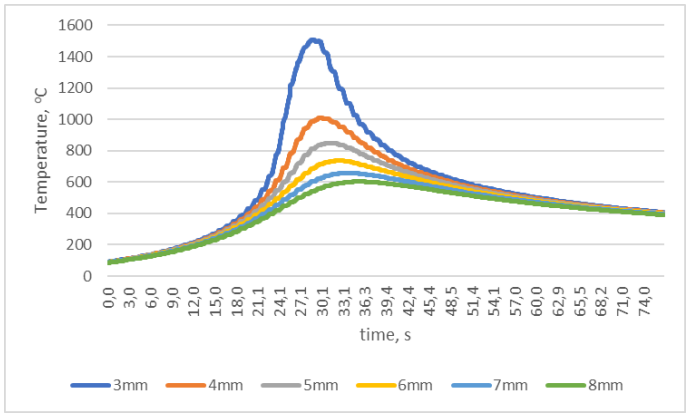


Fig. 4 *Measured contact temperature by Spider 8.*

4. *References*

1. H. Dong ; M. Cong ; Yu. Zhang; Yu. Liu ; H. Chen, Real time welding parameter prediction for desired character performance, IEEE International Conference on Robotics and Automation (ICRA), 2017
2. E. Karadeniz, U. Ozsarac, C. Yildiz. The Effect of Process Parameters on Penetration in Gas Metal Arc Welding Process. Materials and Design. 28(2):2007; 649–656.
3. P. Tashev, „Modeling of temperature processes in automated TIG welding overlay and samples with plain surface“, Collection of reports, Vth National conference with foreign participation „„„Metal science, hydro- and aerodynamics and national security ’2015“, 22 – 23 October 2015, Sofia, ISSN 1313-8308
4. P. Ghosh, S. Gupta, P. Gupta, R. Rathi, Fatigue Characteristics of Pulsed MIG Welded Al-Zn-Mg Alloy. Journal of Material Science. 26(22):1991; 6161–6170.
5. N. Takuo, M. Takashi, K. Katsuhiro, Deformation and Fatigue Characteristics of Large Welded Bellows with Inclined External Edge, Materials Transactions, Vol. 49, No. 6 (2008) pp. 1249 to 1255, 2008 The Japan Society for Technology of Plasticity
6. I. Kim, M. Park, A Review on Optimizations of Welding Parameters in GMA Welding Process, Journal of Welding and Joining, Vol. 36, No. 1, 2018, pp. 65-75, ISSN 2466-2232
7. V. Chauhan, G. Khandoori, A. Kumar, Role of Taguchi Design of Experiment in Optimization of Welding Process Parameters for Different Materials-A Review. International Journal of Advanced Technology & Engineering Research (IJATER). 2014; 146–151
8. D. Kim, M. Kang, S. Rhee, Determination of Optimal Welding Conditions with a Controlled Random Search Procedure. Welding Journal. 2005
9. G. Posch, J. Bruckner, H. Ennsbrunner, INDUSTRY 4.0 IN WELDING, Fronius International, 2017
10. P. Hammersberg, H. Olsson, Proactive Control of Weld Dimensions in Robot MAG Welding. 2013
11. P. Tashev, A. Tasev, M. Manilova, Ya. Lukarski, Methodology for defining technological parameters of resistance welding of cross wires, VIth International Metallurgical Congress, Ohrid 2014
12. https://play.google.com/store/apps/details?id=com.kemppi.arcmobilecontrol&hl=en_US
13. https://www.boschrexroth.com/en/xc/products/product-groups/welding-technology/controllers-with-power-section/mf-system-prc7000/prc7300/prc7300-2
14. http://www.linde-gas.com/en/products_and_supply/welding_safety_products/digital-welding-management/index.html